Dynamic Stall and Virtual Camber on High-Solidity Vertical Axis Wind Turbines

Preprint · August 2025

DOI: 10.13140/RG.2.2.17320.43529

2 authors, including:

David Greenblatt
Technion – Israel Institute of Technology
205 PUBLICATIONS **5,676** CITATIONS

Dynamic Stall and Virtual Camber on High-Solidity Vertical Axis Wind Turbines

Yair Reingewirtz and David Greenblatt
Faculty of Mechanical Engineering, Technion – Israel Institute of Technology

Abstract

The effects of dynamic stall and virtual camber were studied experimentally on 2- and 3-bladed vertical axis wind turbine models, with NACA 0021 blade profiles, corresponding to chord-to-radius ratios of 0.75 and 0.5, respectively, thereby enforcing constant solidity. Open jet wind tunnel measurements were performed in the wind speed range 4.0 m/s to 8.2 m/s, where torque and phase-resolved blade surface pressure measurements were made simultaneously. The 2-bladed average peak torque and power exceeded those of the 3-bladed configuration, by approximately 32%, primarily due to delayed dynamic stall, caused by increased blade pitch rates, which are linearly proportional to the chord-to-radius ratio. However, the unsteady turbine drag loads of the 2-bladed configuration were 92% higher. Virtually all positive torque was developed in the upwind quadrants, consistent with previous studies, and the moments developed around the strut-blade connection point, which are usually neglected, constituted a significant fraction of the total torque developed. Virtual camber was studied by computing the pressure coefficient distributions on a conformally cambered airfoil and then comparing them to measured pressure coefficients at corresponding angles-of-attack. The close correspondence between measurements and calculations represents the first unambiguous experimental confirmation of virtual camber. The strut-blade connection point, between 40% and 60% chord, had a profound effect on the nature of torque generation, but not the cycle-averaged values. A connection point of 50% chord proved to be optimal, because it produced the lowest unsteady and mean, drag and lateral, forces on the turbine.

Keywords: renewable energy, wind energy, vertical axis wind turbine, VAWT, dynamic stall, virtual camber.

1 Introduction

Lift-based vertical axis wind turbines (VAWTs) appear to have advantages over their horizontal axis counterparts due to their relatively low noise emissions, insensitivity to wind direction, and ground-level location of the drive train [1-3]. Despite these ostensible advantages, large-scale VAWTs historically suffered from relatively low energetic efficiency, inability to self-start, as well as fatigue failure of blade connections and drive-train components [4-6]. The mechanical failures derived from their inherent unsteady operation, where large cyclic loads are imposed on the structure. Moreover, near peak power, the blades are routinely subjected to the phenomenon of dynamic stall, that significantly increases the peak loads [7].

In contrast to large-scale turbines, multibladed lift-based small-scale (<100 kW) high-solidity VAWTs can overcome the problem of self-starting and are suitable for high-torque applications [8-10]. We define high-solidity as $\sigma \equiv N\varepsilon > 1$, where N is the number of blades and $\varepsilon \equiv c/R$ is the chord-to-radius ratio. High-solidity also translates to low rotational speeds ω—commonly expressed as the blade tip-speed ratio $(\lambda \equiv \omega R/U_\infty)$—which results in smaller unsteady loads, lower noise emissions [11], and increased bird safety [12,13]. The downside is that their energetic efficiencies are relatively low, i.e., power coefficients rarely exceed 30% [14-17]. Two important factors that must be accounted for are dynamic stall and "virtual camber," and the combination of N and ε that produce the identical solidity, strongly influence both of these factors [18]. For dynamic stall, the dimensionless pitchrate is dependent on ε, and this affects the well-known lift overshoot [19-21] associated with dynamic stall. For virtual camber, larger ε translates to larger differences between flow conditions at the leading- and trailing-edges [18,22-26]. For a given solidity, fewer blades with larger chord-lengths bring both advantages and disadvantages. Advantages include higher blade Reynolds numbers, which generally improve aerodynamic performance [15,27], and proportionately thicker blades that increase structural stiffness [35,27]. Disadvantages are that fewer blades negatively impact self-starting and increase impulsive unsteady loads [7].

The analysis and design of VAWTs is based in either the Blade-Element Momentum (BEM) method [3,7], or the Lifting Line Free Vortex Wake (LLFVW) method [28,29]. For both methods, accurate estimates of the blade lift and drag coefficients throughout the cycle are required for accurate performance and load predictions. For high-ε turbines, this means that the combined effects of dynamic stall and virtual camber must be accurately accounted for. At present, there is insufficient physical understanding of the combined effects to include them successfully into analysis and design methods. This research aims to bridge this gap by directly

measuring and phase-averaging surface pressures on 2- and 3-bladed high-ε turbines, in combination with conventional turbine dynamometry. It is well known that pressure coefficient distributions accurately reflect the flow state [30], and hence they are used as a diagnostic tool and well as a guide for the development of analysis and design tools. In contrast to many other studies, we maintain constant turbine solidity, irrespective of the number of blades. This avoids the problem of varying two parameters, namely blade number and solidity, simultaneously.

The specific objectives are: (i) to study the role of dynamic stall in torque generation; (ii) to identify and quantify the effects of virtual camber during routine operation; and (iii) to quantify unsteady drag and lateral loads acting on the turbine. With greater understanding of the aerodynamics, new methods and strategies can be developed to improve turbine performance, reduce unsteady loads, and provide accurate load inputs for design. The remainder of the paper is structured as follows: The concepts of virtual camber and dynamic stall, within the context of high-solidity VAWT, are reviewed in section 2. The experimental facilities and test turbines are described in section 3, followed by the results, analysis and discussion presented in section 4. Finally, the main conclusions are summarized in section 5.

2 Virtual Camber and Dynamic Stall

The analysis of high-ε turbines must account for both virtual camber [22-24] and dynamic stall [18,25,31,32]. Virtual camber is quantified based on the upwind, torque-producing, half of the azimuth shown in Figure 1, where V_b is the blade speed at the strut-blade connection point x_c, U_i is the induced velocity (assumed temporally constant and constant across the turbine diameter D) and W is the velocity relative to the blade at x_c [18,26]. From the kinematics, the nominal angle-of-attack at x_c is:

$$\alpha_n = \tan^{-1}\left(\frac{\sin\theta}{\lambda^+ + \cos\theta}\right) + \beta, \tag{1}$$

where $\lambda^+ = \lambda/(1-\bar{a})$, the average induction factor $\bar{a} \equiv 1 - \bar{U}_i / U_\infty$ and β is the physical offset angle. From the blade kinematics, the virtual camber-line slope is:

$$dz'/dx = \tan^{-1}\left(\frac{\sin(\theta+\beta')}{\lambda^+ + \cos(\theta+\beta')}\right) - \tan^{-1}\left(\frac{\sin\theta}{\lambda^+ + \cos\theta}\right) - \beta' \tag{2}$$

where the virtual offset angle:

$$\beta' = \tan^{-1}\left(\frac{x_c - x}{c}\frac{c}{R}\right) \tag{3}$$

The corresponding relative dynamic pressure along the chord-length is:

$$q_{\text{rel}} \equiv \tfrac{1}{2}\rho|W|^2 = \tfrac{1}{2}\rho U_\infty^2\{[\lambda^+ + \cos(\theta+\beta')]^2 + \sin^2(\theta+\beta')\} \tag{4}$$

and the nominal dynamic pressure at x_c, is $q_{\text{rel},n} = q_{\text{rel}}(\beta' = 0)$. In the blade-element momentum method, the average induction is calculated iteratively by applying conservation of mass and momentum across the turbine, and equating this to the calculated or measured loads on the blades [3,7]. The LLFVW method, on the other hand is time dependent, where each blade is represented as a lifting line, and the wake is modeled as discrete vortex filaments that are shed from the trailing edge at each time step—affected by their own induced velocity and the velocity induced by other filaments (Biot–Savart law)—and the freestream [28,29]. Using the LLFVW method, it was shown that the disparity between virtual camber effects increase with increasing ε.

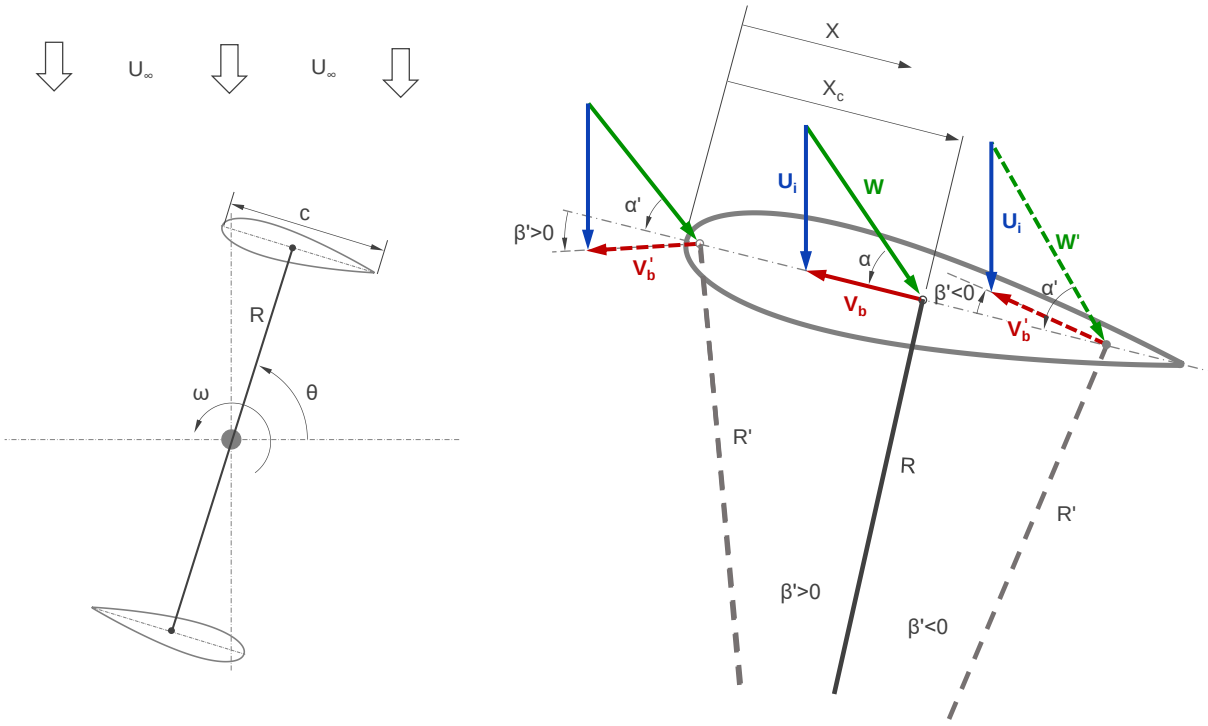

Figure 1. VAWT blade schematic showing the relevant geometric and angular definitions (left), with corresponding idealized velocity components and virtual angles on the upwind blade (right).

The dynamic stall process produces the vast majority of torque on high-ε VAWTs when $\lambda \approx 1$. This is because the static lift overshoot occurs during pitch-up, when the relative dynamic pressure is high, while shedding of separated-flow vortices occurs when the dynamic pressure is low. Thus, in the absence of some flow control device or method, the problem becomes one of managing the dynamic stall process to maximize efficiency and reduce unsteady loads. Furthermore, the vast majority of useful torque is produced in the upwind quadrants, while the downwind quadrants can even produce negative net torque [27,33,34]. At the strut-blade connection point (i.e., nominal conditions), the dimensionless pitchrate rate is defined as:

$$\kappa \equiv \dot{\alpha}_n c / 2|W| \tag{5}$$

To estimate this parameter during the pitch-up motion, we let $\theta = \omega t$ and differentiate equation (1) with respect to time, to yield the nominal blade pitch-rate at x_c / c, namely:

$$\dot{\alpha}_n \equiv \frac{d\alpha_n}{dt} = \frac{\omega(\lambda^+ \cos\theta + 1)}{(\lambda^+)^2 + 2\lambda^+ \cos\theta + 1} \tag{6}$$

Substituting equation (6) and the absolute value of W from equation (4) into equation (5), results in:

$$\kappa = \frac{\varepsilon}{2} \frac{\lambda^+(\lambda^+ \cos\theta + 1)}{(\lambda^+)^2 + 2\lambda^+ \cos\theta + 1 \sqrt{\left(\lambda^+ + \cos\theta\right)^2 + \sin^2\theta}} \tag{7}$$

Finally, for small values of θ (typically valid up to 100°), equation (7) reduces to the approximate relation:

$$\kappa_{\text{up}} \approx \frac{\varepsilon}{2} \frac{\lambda^+}{(\lambda^+ + 1)^2} \tag{8}$$

which is linearly dependent on ε and weakly dependent on λ^+ around unity. This is a useful result because it implies that wind tunnel data acquired on airfoils subjected to constant pitch-rate rotation [19,20]—and not harmonic pitch oscillations—are directly relevant to high-ε aerodynamics. When this is taken into account, together with the weak dependence of virtual camber on θ, then unsteady aerodynamics associated with suitably cambered airfoils under constant pitchrate motion are appropriate for turbine analysis.

The above relations are used to compare the relevant parameters for two configurations considered here, namely $N = 2$ $(\varepsilon = 0.75)$ and $N = 3$ $(\varepsilon = 0.5)$, with identical solidities $\sigma = 1.5$, where peak power is attained at $\lambda \approx 1$ [18]. For illustrative purposes we assume that $\bar{a} = 0.2$ (i.e., less than the Betz limit, $\bar{a} = ⅓$), which yields $\lambda^+ = 1.21$, and that blade static-stall angle $\alpha_s = 20°$. Variation of the parameters with azimuthal angle is shown in Figure 2, where the shaded area on the graph corresponds to post-static-stall angles-of-attack. It is clearly evident that the blades exceed the static stall angle for the major sector of the upstream quadrants. Note, that under these idealized conditions, the difference between the two configurations is the dimensionless pitch-rate κ, which is larger by a factor of 1.5 for $N = 2$. It is anticipated that larger κ will bring about larger peak lift coefficient overshoots, and hence greater turbine performance. It is also expected, from the figure, that very little useful torque will be generated for $\theta > 150°$ due to the relatively low dynamic pressure.

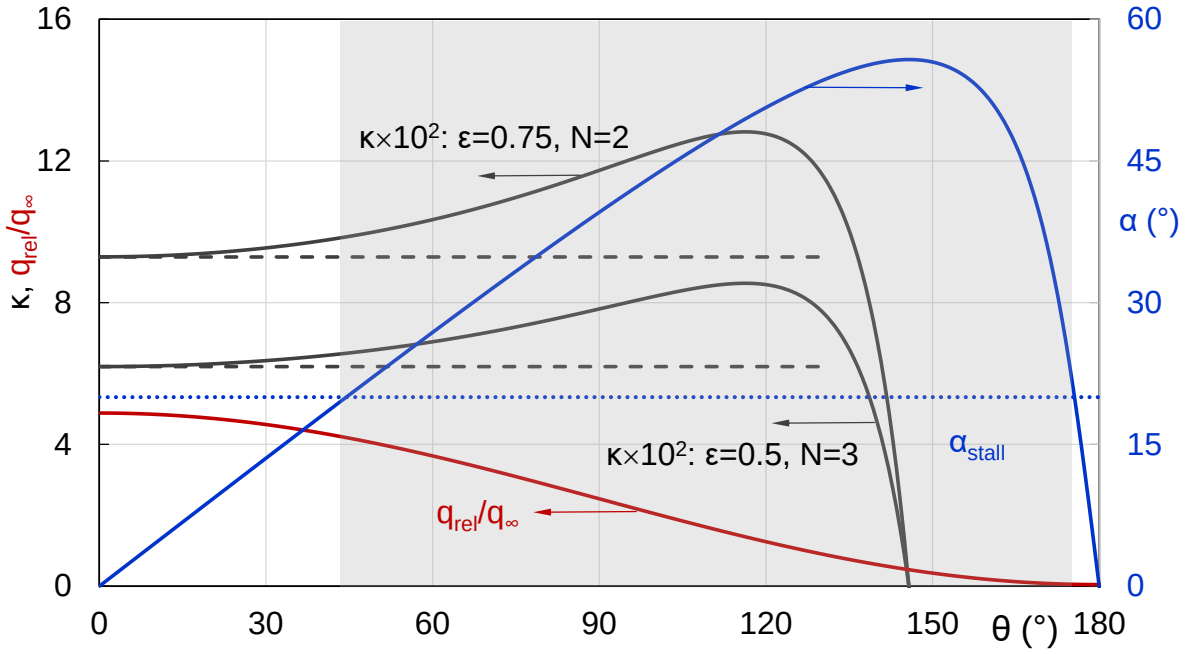

Figure 2. Variation of nominal angle-of-attack, dimensionless pitch-rate and relative dynamic pressure in the upwind quadrants for $N=2$ and $N=3$ configurations ($\sigma=1.5$), under the assumption $\bar{a}=0.2$, which yields $\lambda^{+}=1.21$ (see equations (2) to (4)). The corresponding κ_{up} values, calculated from equation (8), are shown as the black dashed lines. The shaded area represents post-stall angles-of-attack for $\alpha_s=20°$.

3 Experimental Facilities and Test Turbines

3.1 Wind Tunnel & Test Turbine Configurations

Experiments were performed using a test turbine mounted downstream of an open jet produced by a blowdown wind tunnel [18,26], shown in Figure 3. The tunnel is driven by a 75-kW centrifugal blower, attached to a large-angle diffuser, plenum and double-nozzle with an overall contraction ratio of 2.6. The plenum is equipped with course turbulence reduction grids and an anti-swirl mat. The jet exit area has dimensions 1.0 m (height) × 1.9 m (width), with a maximum wind tunnel velocity of $U_\infty = 16$ m/s, a relative standard deviation distortion of 1.4% and a turbulence level $Tu = 0.5\%$. The wind tunnel velocity is measured by means of Siemens QBM3020-1U 50 pascal pressure transducers.

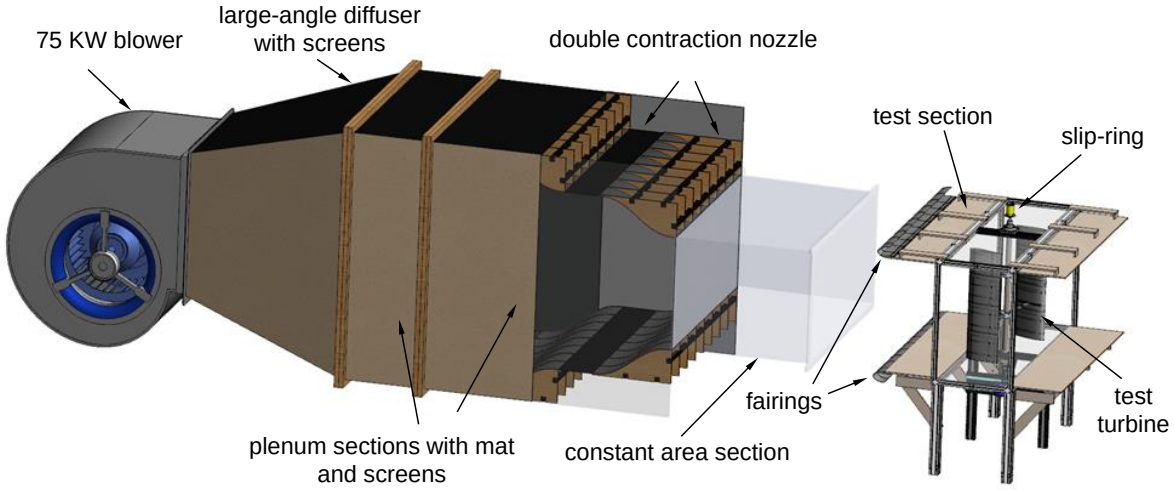

Figure 3. Schematic of the blowdown wind tunnel and separate test section housing the test turbine.

The test turbine was mounted in the center of a separate 1.56-meter-long test section, with the sidewalls removed, and with 10 cm elliptic airings on the upstream floor and ceiling part as shown in Figure 4. The turbine comprised a stainless-steel hollow shaft (diameter $d = 50.6$ mm), mounted on UC-210 self-aligning bearings above and below the test section. Aluminum shaft-adapters, for accommodation of the blade-struts, were mounted equidistant (300 mm) from the test section floor and ceiling. Two sets of adapters were designed to accommodate either two-bladed or three-bladed configurations, referred to as $N = 2$ and 3 configurations, respectively. (The design allowed for the accommodation of blade adapters for an arbitrary number of blades.) Stainless-steel strut segments, of various lengths, were used to connect the blades to the shaft adapters, and different combinations of segments were

concatenated in order to produce the desired turbine radius R. NACA 0021 blades were employed, with chord-lengths $c = 300$ mm, span-lengths $b = 970$ mm and trailing-edge thicknesses of 2 mm. Radii $R = 0.4$ m and 0.6 m, respectively were employed, in order to produce $\sigma = 1.5$ for the $N = 2$ and 3 configurations, and the projected area was defined as $A \equiv 2Rb$. The small gap between the tips and the floor or ceiling ($g = 15$ mm), expressed in dimensionless form as $g/c = 0.05$ or $g/b = 0.016$, ameliorated tip-loss effects [35,36].

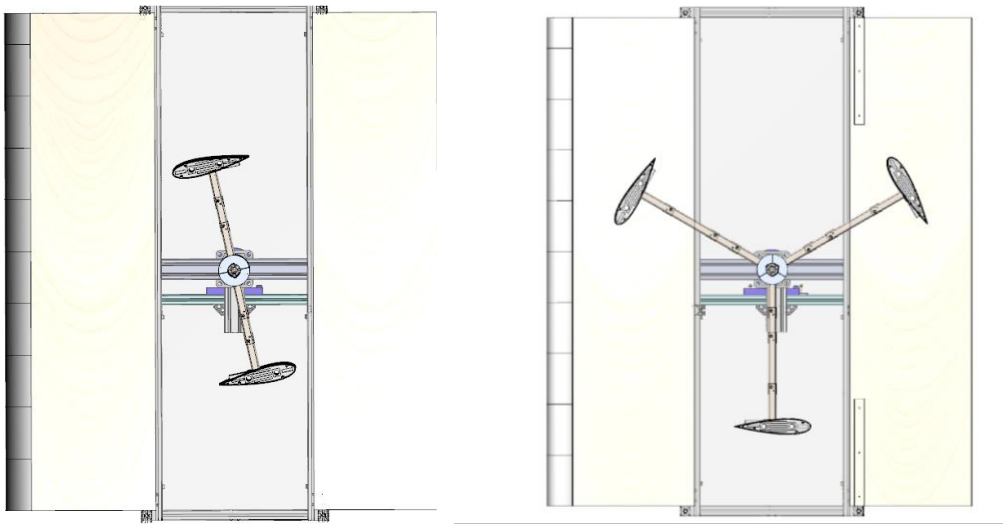

Figure 4. Cross-sectional plan views at the upper strut-blade connection height showing the two-bladed ($N = 2$, left) and three-bladed ($N = 3$, right) configurations, where $\sigma = 1.5$ in both cases. Wind flows from left to right.

The load-bearing assembly of each blade was comprised of two aluminum ribs that were bolted to two 20 mm diameter carbon fiber spars. The inboard sides of the ribs were equipped with 16, 5 mm holes with stainless-steel helicoil insert threads. These were connected to the struts using small flanges, which facilitated variation of the strut-blade connection point in the range $0.13 \le x_c/c \le 0.63$ (see Figure 5). Six additional ribs, used to maintain the integrity of the blade geometry, were 3D printed from Polylactic Acid (PLA) and screwed into the spars. The outer shell of each blade comprised four 2 mm thick 3D printed PLA segments. The segments were manufactured with mating slots and glued together. The shell assembly was then screwed to the eight (two aluminum and Six PLA) ribs. One blade was equipped with a pressure-port module, described below in section 3.2.

3.2 Dynamometry & Pressure Measurements

The turbine was loaded using a custom dynamometer, that comprised an HB-140M2 Magtrol 10 Nm hysteresis magnetic brake and a Kistler 4502A10RAU (10±0.02 Nm) torque meter (see Figure 5). Torque was transmitted to and from the torque meter via two sets of flexible couplings. The average rotational speed (f) was measured using a KFPS TL proximity sensor as a tachometer, facilitating the calculation of the average power $\bar{P} = \bar{T}\omega$, where $\omega = 2\pi f$, and overbars indicate time-averaged values. Turbine performance and surface pressure experiments were performed simultaneously in the wind tunnel velocity range $4.0\ \text{m/s} \le U_\infty \le 8.2\ \text{m/s}$ (± 0.15 m/s). The data acquisition system was controlled using a dedicated LabVIEW© program. The brake loading was generated automatically via a TTI CPX400DP programable power supply while acquiring real-time measurements from the various sensors. The loading torque was varied in steps of $0.005\ \text{Nm} \le \Delta T \le 0.02\ \text{Nm}$, and all data were acquired for 60 to 240 seconds when the rotational speed reached a nominal steady-state, namely, standard deviation to average ratio less than 0.2%.

The total average parasitic frictional torque $\bar{T}_{\text{par}}$, i.e., in the bearings and slip-ring, was determined by removing the blades and struts, and replacing the brake with a 0.75 kW servo motor. The torque was then recorded while rotating the shaft at the rotational speeds obtained in the experiments.

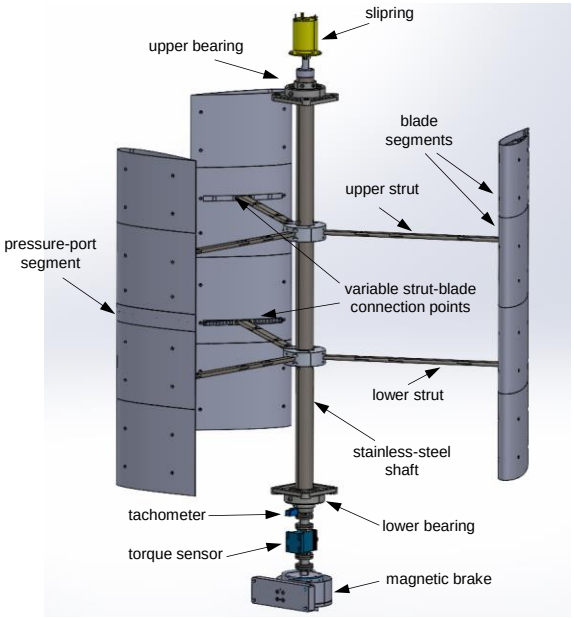

Figure 5. Schematic rendering of the 3-bladed turbine model configuration, with the test-section removed, showing the main components.

One blade was equipped with pressure ports, at the center-span location, connected to an internally mounted pressure scanner. This was done by shortening one inner segment by 50 mm and replacing it with a corresponding 50 mm wide (span) pressure-port segment, using identical mating slots as those described above. The pressure-port segment was equipped with 32 pressure ports, constructed from stainless-steel tubing—16 and 14 ports were located on the inner and outer surfaces respectively, and one each at the leading- and trailing-edges. The pressure ports were connected internally to a 32-port, 10 in WC (250 pascal), ESP-32HD electronic differential pressure scanner, by means of 200 mm long vinyl tubing. The reference (static pressure) port was threaded along a top strut and through the shaft to a port in the center of the shaft external to the test section. The ESP data acquisition and communication cable was threaded in the same way and attached to a 16-channel Moflon MT-2069F–S16-VH slipring mounted above the shaft, outside of the tunnel. The ESP pressure module was triggered using an Agilent 33210a function generator that, in turn, was triggered by a proximity sensor.

To provide a comparison between turbine blade pressures and the corresponding static pressure distributions, static blade pressure measurements were made at 2.5° increments using a custom-designed bracket. These measurements were made at a wind speed of 11 m/s in order to obtain similar Reynolds numbers to those experienced during turbine operation.

4 Results, Analysis and Discussion

4.1 Performance Characteristics

The overall performance characteristics of the 2-bladed and 3-bladed ($N=2$ and $N=3$) configurations were evaluated using both the custom dynamometer and by the integration of the phase-averaged blade surface pressures. Upon reaching steady-state conditions defined in section 3.2, phase-averaged pressures based on 60 or 240 turbine cycles produced results with negligibly small differences, typically less than several pascals. Hence the majority of phase-averaged results were based on 60 turbine cycles. Following phase-averaging, blade surface pressures at equally spaced points on the blade surface $p(s_i,\theta_k)$ were linearly interpolated from the two adjacent pressure ports $P(S_j,\theta_k)$ and $P(S_{j+1},\theta_k)$. Here, s_i and S_j represents the distance along the blade contour from the leading-edge, where $i=1,...,1,000$ and $j=1,...,32$, and θ_k is an arbitrary phase angle. At each s_i, the normal to the surface $\hat{n}_i$ was calculated from the blade geometry, and s_i were expressed in terms of the blade coordinates (x_i,z_i), and thus for $s_i \in (S_j,S_{j+1})$, the interpolated pressures are calculated by:

$$p(s_i,\theta)=\frac{P(S_{j+1},\theta_k)(s_i-S_j)+P(S_j,\theta_k)(S_{j+1}-s_i)}{S_{j+1}-S_j} \tag{9}$$

This facilitated direct calculations of the tangential and radial force components:

$$\tilde{F}_{t,i}(\theta)=p(s_i,\theta_k)\cdot\hat{n}\cdot\hat{x} \tag{10}$$

$$\tilde{F}_{r,i}(\theta)=p(s_i,\theta_k)\cdot\hat{n}\cdot\hat{y} \tag{11}$$

as well as the moment about the strut-blade connection point:

$$\tilde{M}_i(\theta_k)=\tilde{F}_t(\theta_k)\cdot y_i+\tilde{F}_r(\theta_k)\cdot(x_i-x_c) \tag{12}$$

Hence, the phase-dependent forces and moments acting on the blade were calculated according to $F_t(\theta_k)=\Sigma\tilde{F}_{ti}(\theta_k)$, $F_r(\theta_k)=\Sigma\tilde{F}_{ri}(\theta_k)$, and $M(\theta_k)=\Sigma\tilde{M}_i(\theta_k)$, and the torque due to tangential forces according to $F_t(\theta_k)\cdot R$. Finally, the cycle-averaged torque was calculated by:

$$\bar{T}=\frac{1}{N_c}\sum_{k=1}^{N_c}\left(M(\theta_k)+F_t(\theta_k)\cdot R\right) \tag{13}$$

where the number of points in each cycle N_c varied between 110 and 150.

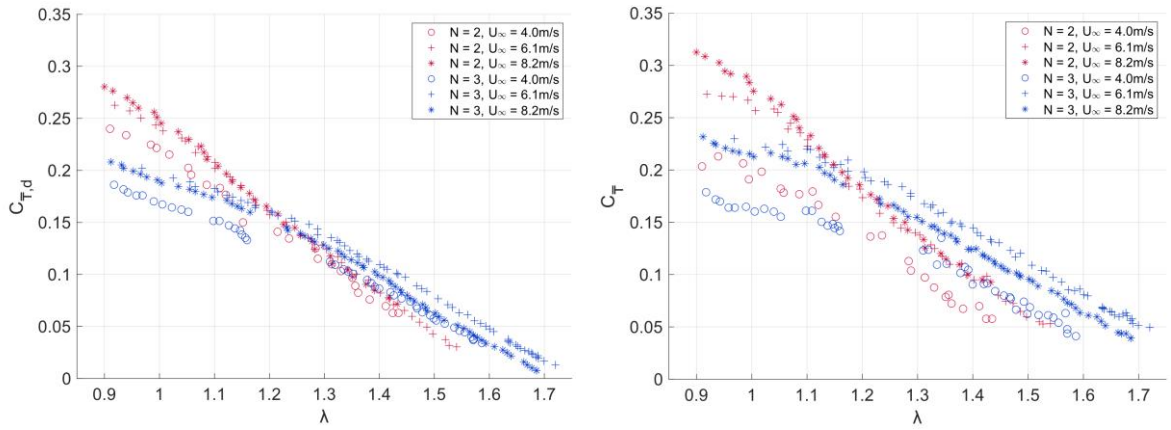

Figure 6. Average turbine torque coefficients as a function of tip-speed ratio for the $N=3$ and the $N=2$ configurations. Left: Experimental results based on dynamometer measurements. Right: Experimental results based on the integration of blade surface pressures.

The average torque coefficients based on dynamometer and integrated surface pressures, ($C_{\bar{T},d} \equiv (\bar{T}_d + \bar{T}_{\text{par}})/q_\infty AR$ and $C_{\bar{T}} \equiv \bar{T}/q_\infty AR$, respectively), are shown as a function of tip-speed ratio ($\lambda \equiv \omega R/U_\infty$) in Figure 6, for freestream wind speeds $U_\infty = 4.0$ m/s, 6.1 m/s, and 8.2 m/s. The dynamometer-based measurements are on the left and the integrated surface pressure results are on the right, where the latter, which was based on equation (13) was multiplied by either $N=2$ or 3, depending upon the configuration. The results for all configurations and wind speeds show consistent trends. First, there is a general increase in maximum torque coefficient for wind speeds exceeding 4 m/s. This is most likely a Reynolds number effect, where $Re_{\max} \equiv U_\infty(1+\lambda)c/\nu$ at $U_\infty = 4.0$ m/s and 8.2 m/s correspond to 1.6×10^5 an 3.3×10^5. It is well known that both airfoil aerodynamic efficiency C_l/C_d and maximum lift $C_{l,\max}$ reduce when Reynolds numbers are less than 2×10^5 [37,38]. Second, the $N=2$ configuration consistently produces greater peak torque, while the $N=3$ configuration produces greater torque at higher blade tip speeds, and this results in a "crossover" of the results. These performance differences are clearly not due to solidity or Reynolds number effects, because both are nominally the same. The differences must therefore be ascribed to the dynamic stall effects, virtual camber effects, or both—as discussed in section 2—i.e., due to differences in the parameter $\varepsilon \equiv c/R$.

The side-by-side comparison of the two results in Figure 6, shows that the integrated pressure results are generally larger than the dynamometer results. This is primarily because the net pressure integration neglects viscous drag and also does not account for tip effects.

During the experiments, it was noted that data points corresponding to $U_\infty = 4.0$ m/s took longer to converge and showed larger scatter when compared to the data at $U_\infty = 6.1$ m/s and 8.2 m/s. These data were considered to be less reliable and/or accurate and were were not considered for further analysis of the turbine blade aerodynamics.

Turbine average power coefficients ($C_{\bar{P},d} \equiv \bar{P}_d / q_\infty U_\infty A$ and $C_{\bar{P}} \equiv \bar{P} / q_\infty U_\infty A$, respectively) are shown as a function of λ in Figure 7, in the same format as Figure 6. Observations relating to Reynolds number effects, superior performance of the $N = 2$ configuration, and differences in torque measurements, made with respect to $C_{\bar{T}}$ (Figure 6), are valid here too. The nature of the characteristic curves for the two configurations, however, are different. In particular, the $N = 3$ configuration produced a peak-power plateau in the approximate range $0.9 \le \lambda \le 1.2$, while the $N = 2$ configuration appeared to produce a plateau around $0.9 \le \lambda \le 1$. The crossover of the two configurations also occurs consistently at $\lambda \approx 1.15$. We refer to tip-speed ratios corresponding to the plateaus as the design range, because this is where the turbine is intended to operate. The maximum difference between the two configurations in the design range and recorded at $U_\infty = 8.0$ m/s, of approximately 32%, is very significant. Note that values of λ below the design range were not obtained due to our use of a magnetic brake to load the turbine. Lower values can only be obtained with a load such as a variable speed motor, because the turbine torque decreases as the load increases. One repeatable anomaly, for which we have no explanation, is that the $N = 3$ configuration produced higher $C_{\bar{P}}$ values under lower loading, i.e., at larger values of λ, i.e., outside of the design range, at lower wind speed, i.e., Reynolds numbers.

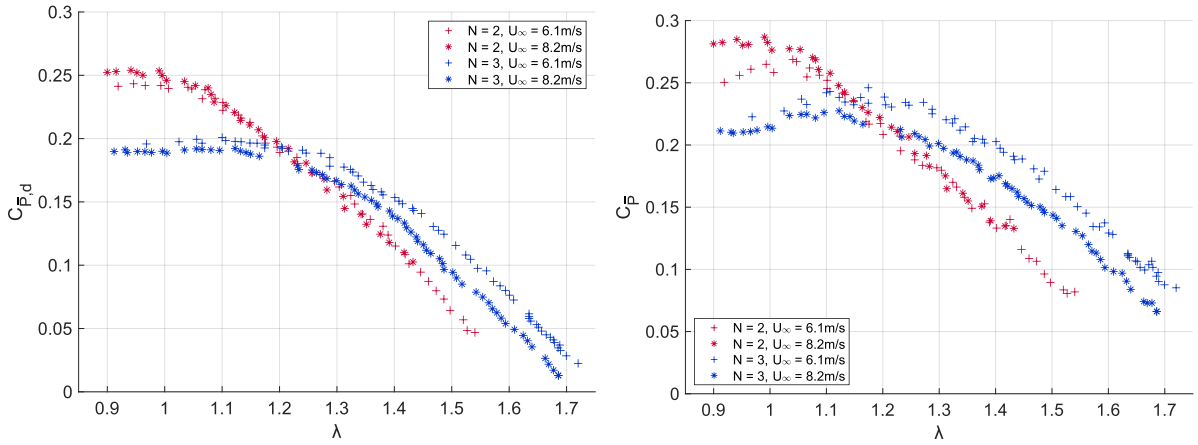

Figure 7. Average turbine power coefficients as a function of tip-speed ratio, for the $N=3$ and $N=2$ configurations. Left: Experimental results based on dynamometer measurements. Right: Experimental results based on the integration of blade surface pressures.

4.2 The Nature of Torque Generation

To better understand the performance differences between the two configurations, the phase-averaged torque measurements were analyzed based on the integration of the blade surface pressures, described in section 4.1. For clarity, the total torque imparted to the turbine is resolved into the component resulting from tangential-loads acting on the blades and the moment about the connection point, namely $T(\theta)=T_t(\theta)+M(\theta)$, where $T_t(\theta)=F_t(\theta)\cdot R$ (see section 4.1). Our estimation of the tangential loads for both configurations is non-conservative, because the retarding viscous effects and tip losses are neglected. This does not materially affect our comparison because these effects are anticipated to be similar for both configurations. Figure 8 shows the two individual components, as well as their sum expressed as the phase-averaged torque coefficients as a function of the azimuthal angle θ, for both configurations, at $U_\infty=6.1\text{m/s}$. In order to provide a meaningful quantitative comparison between the configurations, the single-blade integrated results were multiplied by a factor of either 2 and 3, for the $N=2$ and $N=3$ configurations, respectively. In this way, the integral in both cases corresponds to the average torque coefficient shown in Figure 6 (right). In the discussion that follows, we consider three representative cases, namely: an off-design, relatively high tip-speed ratio case ($\lambda=1.53$); an intermediate tip-speed ratio case, corresponding to the power coefficient crossover region ($\lambda=1.15$); and a low tip-speed ratio case corresponding to the peak power (design) region ($\lambda=0.97$).

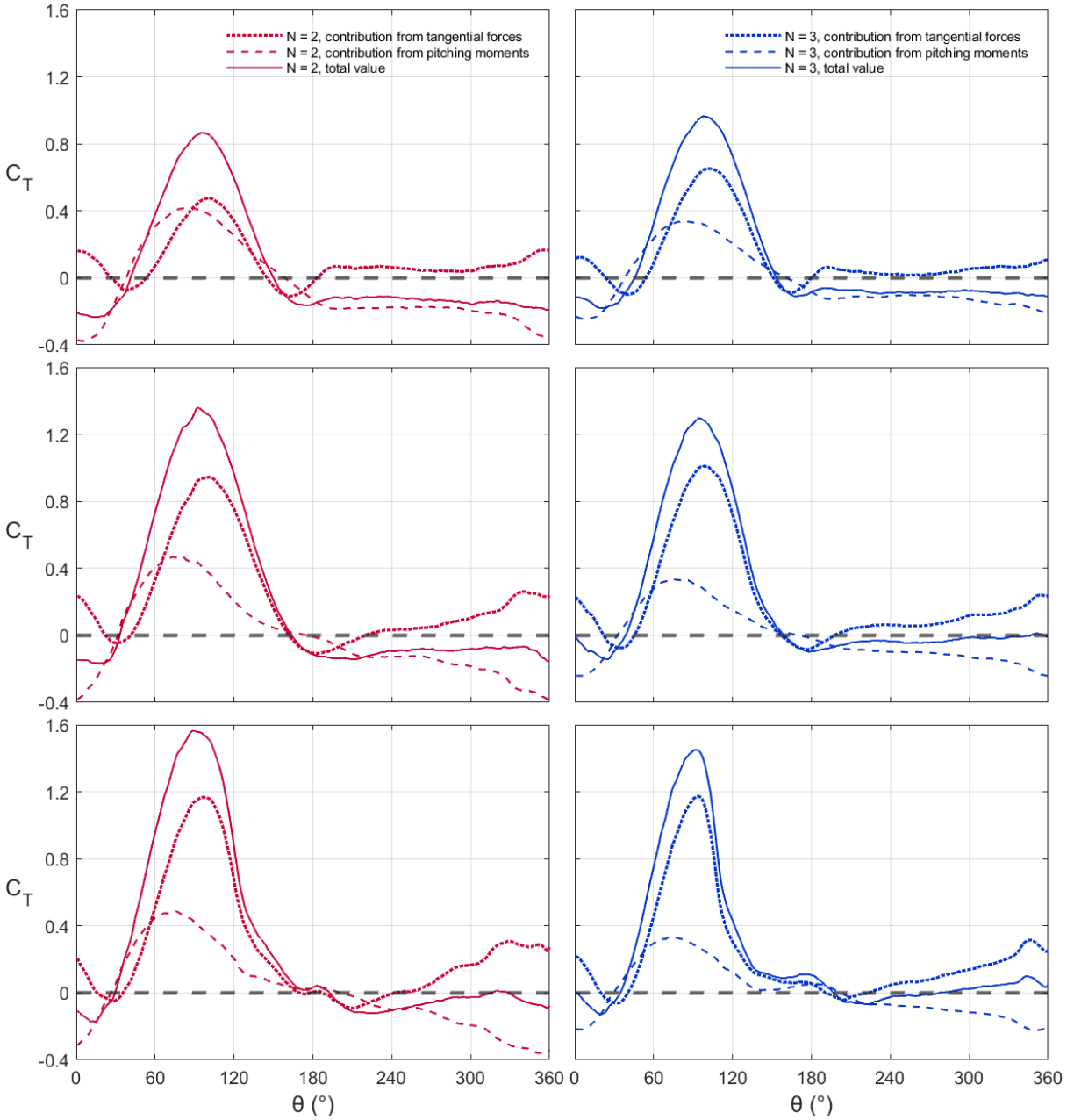

Figure 8. Phase-resolved torque coefficients at $U_\infty = 6.1$ m/s as a function of azimuthal angle in the off-design region ($\lambda = 1.53$, top row), the crossover region ($\lambda = 1.15$, middle- row), and the peak power region ($\lambda = 0.97$, bottom row), for a single blade (left: $N = 2$; right: $N = 3$).

Figure 8 shows that, irrespective of the blade number or tip-speed ratio, virtually all of the useful torque, i.e., $C_T > 0$, is generated in the upwind quadrants, with the lower and upper azimuthal limits around $30° \le \theta \le 50°$ and $130° \le \theta \le 180°$, respectively. At the high tip-speed ratio ($\lambda = 1.53$), where the $N = 3$ configuration produces greater average torque, the peak tangential-load torque component is approximately 35% higher than that of the $N = 2$

configuration, but this is partially offset by the ½-chord moment which is 24% smaller. The $N=2$ configuration furthermore suffers from relatively large pitch-down ½-chord moments (negative, clockwise) in the downwind quadrants, which are approximately double those associated with the $N=3$ configuration. A clearer comparison of the total phase-averaged torque generated can be seen in Figure 9. In the crossover region ($\lambda=1.15$), where the performance of both configurations is comparable, the $N=3$ peak tangential-load torque is slightly greater than that of the $N=2$, but the $N=2$ pitching moment peak is significantly higher, and therefore it attains a higher overall peak. However, in the aft quadrants, the $N=2$ pitching moment again has a larger pitch-down, negative effect, which offsets the higher torque produced in the upstream quadrants. In the peak power (design) region ($\lambda=0.97$), which is by far the most important, both the peak tangential-load torque and the peak pitching moment of the $N=2$ exceed those of the $N=3$—and therefore their sum is significantly greater.

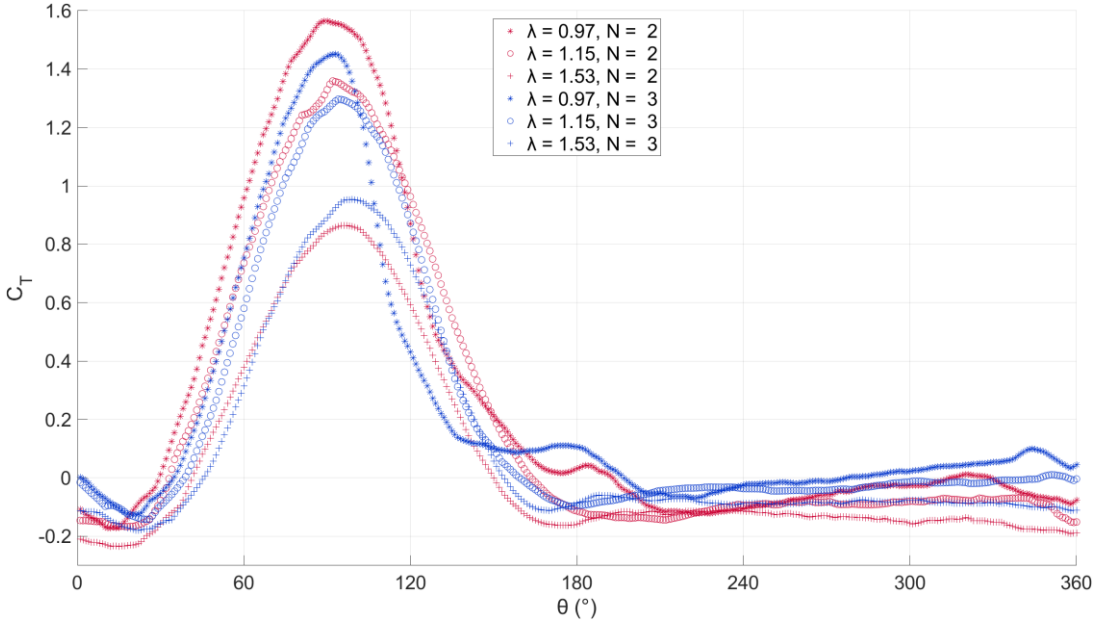

Figure 9. Summary of the total phase resolved torque coefficients as a function of azimuthal angle in the off-design region ($\lambda=1.53$), the crossover region ($\lambda=1.15$), and the peak power region ($\lambda=0.97$), for both turbine configurations at $U_\infty=6.1$ m/s.

Figure 10 shows the average torque coefficients resolved into tangential-load torque and ½-chord moment components, for both configurations, at $U_\infty=6.1$ m/s (left) and 8.2 m/s (right). The vertical lines on Figure 10 (left) indicate the representative λ cases described above. It is evident that, as the turbine is loaded, the negative net effect of the pitching moment decreases linearly with λ and even produces a small positive net effect in the design region. Thus, the

positive pitch-up effect in the upwind quadrants is approximately balanced by the negative pitch-down effect in the downwind quadrants. These results show that neglecting pitching moments, fortuitously, does not have a large effect on the design region performance. However, to accurately predict the entire turbine performance curve, neglecting pitching moments is only justified if $\varepsilon \ll 1$. Equally important, the azimuthally resolved results presented in Figure 8, clearly show that it is beneficial to mechanically offset the negative pitching-moment effects in the downstream quadrants, in order to maximize the turbine performance. This can be achieved, for example, by periodically decambering the blade as it traverses the downstream quadrants. There are at least three ways of doing this: (i) periodically pitching the blades [39]; periodically deflecting trailing-edge flaps [40] or slotted flaps [26]; and periodically morphing the blades. [41,42].

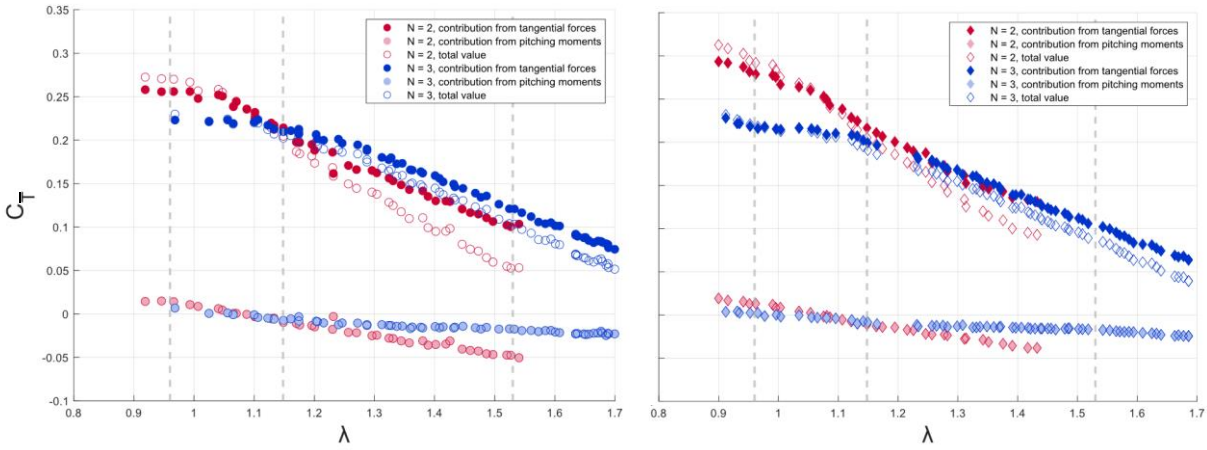

Figure 10. Average torque coefficients based on the integration of blade surface pressures, resolved into tangential-load torque and ½-chord pitching moment components, for the $N = 2$ and the $N = 3$ configurations, at 6.1 m/s (left) and 8.2 m/s (right).

4.3 Blade Pressure Distributions and the Role of Dynamic Stall

The blade pressure coefficient distributions are particularly useful for understanding the nature of the attached and separated boundary layers on the blades. In particular, the quantitative and qualitative distributions allow us to identify the effects of dynamic stall and compare the two configurations. For the purposes of our discussion, we consider the same three representative tip-speed ratio cases described above at $U_\infty = 6.1$ m/s , with pressure coefficient results for the off-design, crossover, and design regions, shown in Figure 11, Figure 12, and Figure 13, respectively. Note that these pressure coefficient distributions are not multiplied by the number

of blades, as was done in Figure 8 and Figure 9. For a quantitative torque generation comparison between the two, the $N=3$ pressure coefficients must be multiplied by 1.5.

For the off-design case ($\lambda=1.53$, Figure 11), the differences between the $N=2$ and $N=3$ configurations are small and quantitative, and hence most of the discussion below applies to both. At $\theta=0°$, the inner and outer pressure distributions are characterized by a crossover at $x/c\approx 0.25$ and 0.3, for the $N=2$ and $N=3$ configurations, respectively. They are nearly symmetric, and hence the tangential-load torque contributions are relatively small (see Figure 8). This, however, is not the case for the pitching moments, because the low pressure outer surface upstream of the crossovers, and the low pressure inner surface pressures downstream of the crossovers, which are weighted by the distance from $x_c/c=0.5$, have the same pitch-down negative (counter clockwise) effect. With increasing azimuthal angle ($\theta=25°$) the higher leading-edge pressures tend to reduce the tangential-load torque, but because the crossover points move forward on the blade, the low-pressure regions move forward, and the pitching moment increases. The pressure distributions are significantly different to those observed on static and dynamically pitching symmetric airfoils and are in fact consistent with a cambered airfoil at negative angles-of-attack (see section 4.4). With further increasing azimuthal angle ($\theta=40°$), the crossover moves to the leading-edge, which significantly increases the pitching moment, and the net effect is that the total torque is close to zero. As the blade progresses further along the azimuth, the low pressures near the leading-edge, combined with the pressure rise along the inner surface, results in a rapid increase in tangential-load torque and less-rapid increase in pitching moment. This produces a relatively flat pitching moment peak at $\theta\approx 80°$ and a sharper tangential-load peak at $\theta\approx 100°$, with their sum in between. The pressures then uniformly decrease and show no obvious sign of flow separation, i.e., dynamic stall. This is due to the combination of rapid pitch rates—the dimensionless pitch-rate only drops by about 4% between $\lambda=0.97$ and 1.53, as shown in equation (8)—and relatively low maximum angles-of-attack associated with this higher tip-speed ratio. Note that at $\theta\approx 180°$, the pressure distributions are qualitatively similar to those at $\theta\approx 0°$ and therefore, by the same reasoning, the pitching moment is again negative.

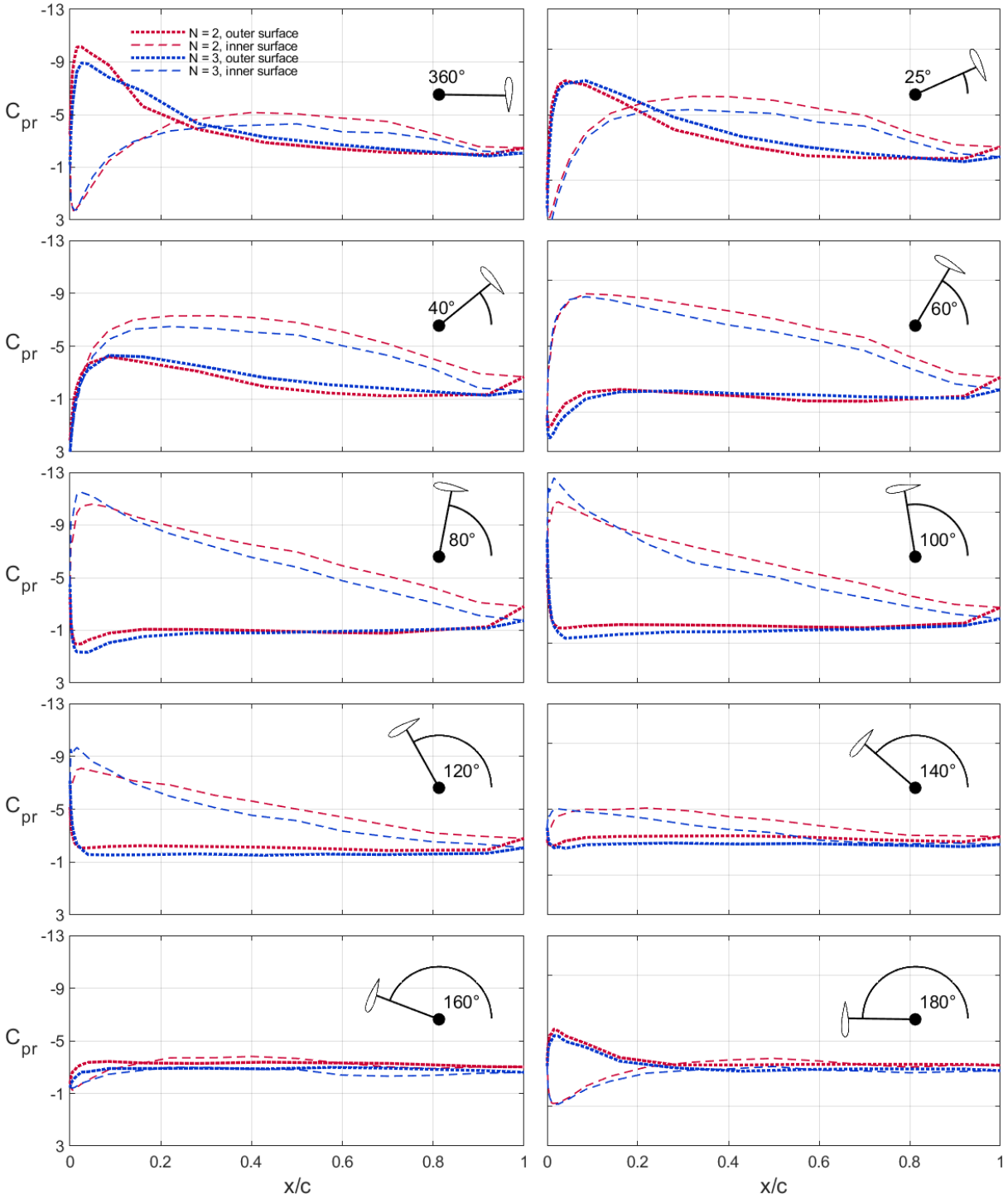

Figure 11. Phase-averaged blade surface pressure coefficients at $U_\infty = 6.1$ m/s for the off-design region ($\lambda = 1.53$), at selected representative azimuthal angles, for both configurations.

For the torque and power crossover region ($\lambda = 1.15$, Figure 12) the pressure distributions at the small azimuthal angles ($\theta \le 60°$) are qualitatively similar to those at $\lambda = 1.53$. However, the pressure crossover points move forward more with θ, and hence positive torque is generated at lower θ (see Figure 8). At larger angles ($80° \le \theta \le 105°$),

separation bubbles are clearly visible on the inner-surface the leading-edge region; these were not visible in the $\lambda = 1.53$ pressure distributions, and are due to the higher nominal angles-of-attack with the increased loading of the turbine (i.e., lower λ). At $\theta = 115°$ there is a clear difference between the $N = 3$ and $N = 2$ leading-edge distributions—the lower pressure downstream of the original $N = 3$ bubble location indicates the onset of bubble bursting, which represents the onset of dynamic stall. The vortical flow associated with bubble bursting is commonly referred to as the leading-edge or dynamic stall vortex (LEV or DSV). In the azimuthal range defined by $105° \le \theta \le 135°$, the $N = 3$ LEV moves downstream to $x/c \approx 0.25$ produces a successively weaker low-pressure region. This should be contrasted with dynamic stall observed on thick airfoils, under nominally constant freestream conditions, where the DSV increases in size and continues to move downstream along the blade chord and subsequently sheds into the wake [43]. On the turbine blade, with increasing azimuthal angles approaching $180°$, the blade and induced velocity magnitudes become comparable and hence there is no mechanism to transport the DSV along the blade chord. The onset of dynamic stall associated with the $N = 2$ is seen to occur at $\theta \approx 125°$. The qualitative result is similar, but because the vortex is shed at a larger azimuthal angle than that of the $N = 3$ configuration, the blade and induced velocities of the $N = 2$ configuration are closer in magnitude and hence the vortex does not move as far along the chord.

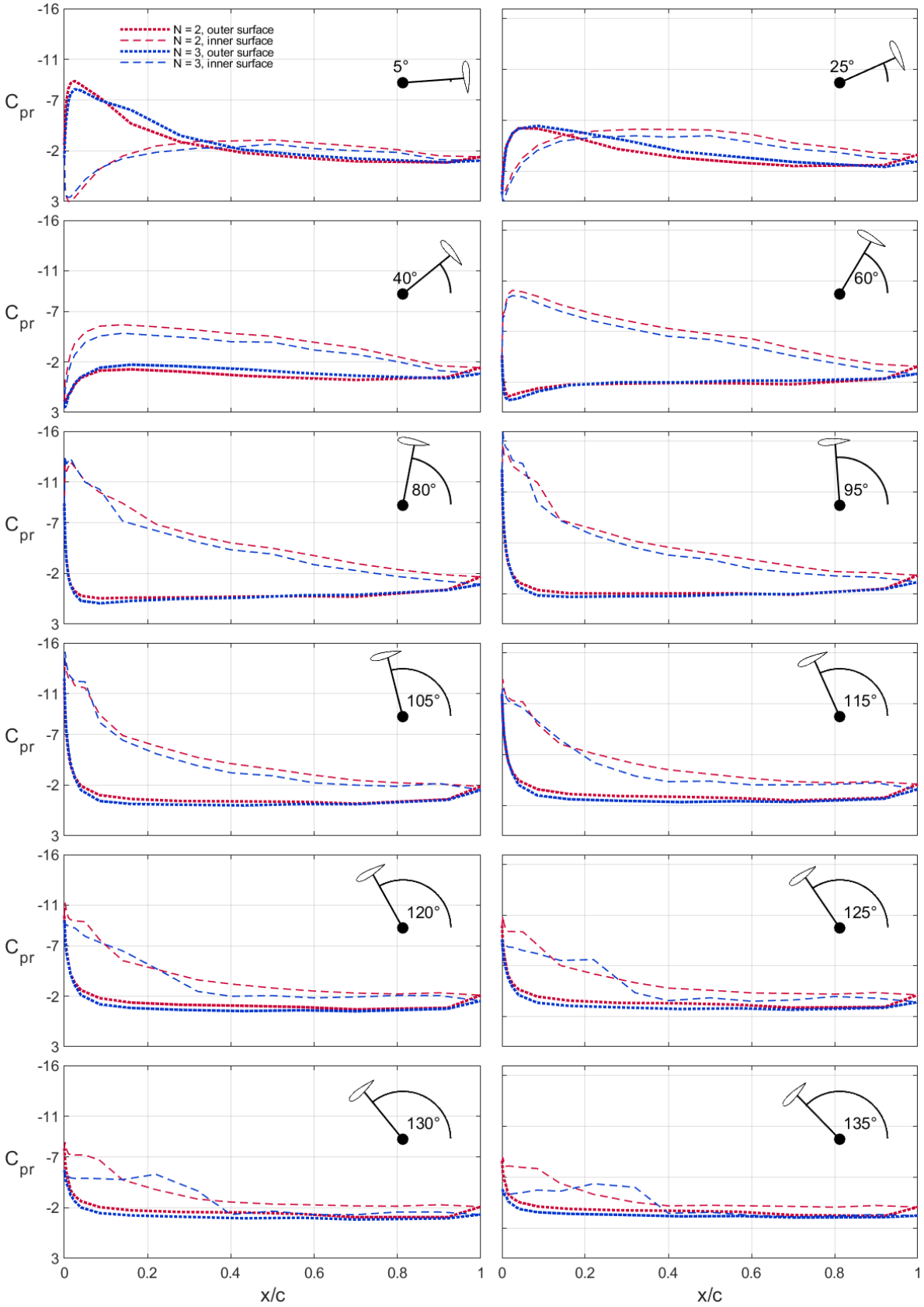

Figure 12. Phase-averaged blade surface pressure coefficients at $U_\infty = 6.1$ m/s for the crossover region ($\lambda = 1.14$), at selected representative azimuthal angles, for both configurations.

Under design conditions ($\lambda = 0.97$, Figure 13), qualitatively similar pressure distributions to those at $\lambda = 1.15$ (Figure 12) are evident until $\theta = 95°$. However, the onset of dynamic stall is evident at lower azimuthal angles, namely $\theta = 100°$ and $105°$, for the $N = 3$ and the $N = 2$ configurations, respectively. The vortex shedding trends are also qualitatively similar, with the $N = 3$ LEV being transported further downstream than the $N = 2$ LEV. By comparing the two latter cases, namely $\lambda = 1.15$ and 0.97, different conclusions can be drawn depending upon the configuration. For the $N = 3$, dynamic stall occurs within our defined design range. Its occurrence at lower azimuthal angles increases the torque coefficient and does not harm the power coefficient. For $N = 2$, the occurrence of dynamic stall at smaller azimuthal angles produces both higher torque and power coefficients.

It is clear from the results presented in Figure 13, that the greater the azimuthal angle of dynamic stall onset, the larger the torque developed by the turbine. Due to the fact that we maintained constant solidity, the delayed dynamic stall and the corresponding increased torque are clearly due to the increased dimensionless pitchrate during the pitch-up motion κ_{up}, which is proportional to ε (see section 2). The design of these turbines, therefore, must model dynamic stall in order to obtain accurate load estimates. It is also self-evident that the passive [44,45] or active [46-48] delay of dynamic stall on VAWT blades can further increase performance, but the discussion of these techniques is beyond the scope of this paper.

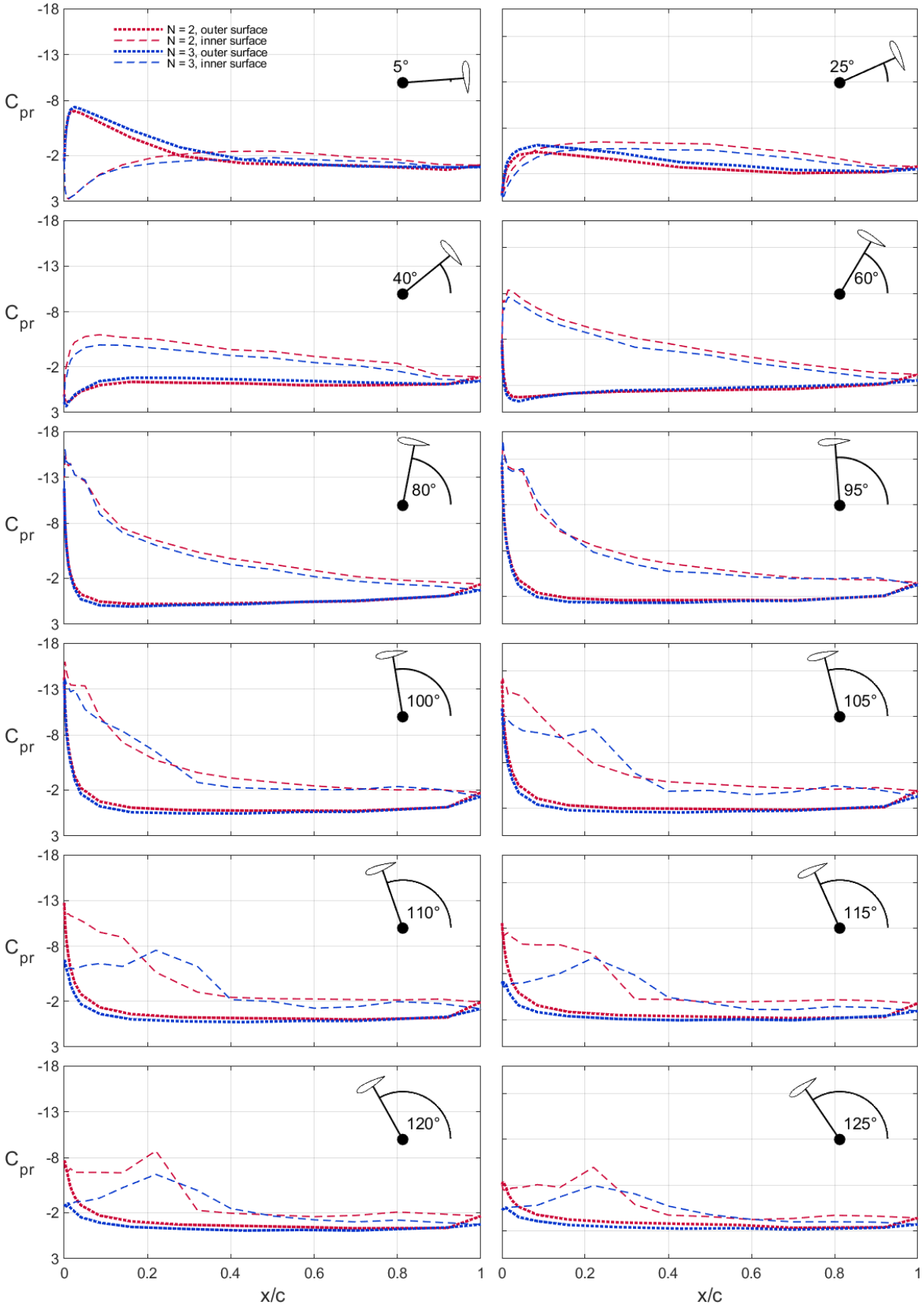

Figure 13. Phase-averaged blade surface pressure coefficients at $U_\infty = 6.1$ m/s for the peak power region ($\lambda = 0.97$), at selected representative azimuthal angles, for both configurations.

4.4 The Role of Virtual Camber

Virtual camber plays an important role in high-ε VAWT turbine aerodynamics but is generally not accounted for in analysis and design. The effects manifest differently in the upwind and downwind quadrants and must be accounted for accordingly. In the discussions below, we focus on the upwind torque-producing quadrants. For a first approximation, we neglect dynamic effects, and we use the simplified blade kinematics, described in section 2, to conformally transform the airfoil geometry. Note, however, that the *aerodynamic problem* cannot strictly-speaking be conformally transformed, because the operation violates conservation of mass. (This may not be the case in parts of the downwind quadrants where $\bar{a} \approx 1$). To account for this violation, we introduce a mass correction term, described below.

To generate the blade shape with virtual camber, we use the virtual camber line, expressed in equations (2) and (3), together with the experimental operation point at $\lambda = 0.97$ and assume that $\bar{a} = 0.2$ (see section 2), which is typical for a VAWT, and gives $\lambda^+ = 1.21$. Under these assumptions, for $\varepsilon = 0.75$ and $x_c / c = 0.5$, we integrate equation (2), which yields $(z'/c)_{\max} \approx 5.0\%$ and 5.3% for $\theta = 0°$ and 70°, respectively (see below), and thus we select a NACA 5521 as representative for our analysis. This, then allows us to calculate the pressure coefficients around both NACA 5521 and 0021 airfoils, and we use the airfoil analysis program Xfoil [49], where $N_{\text{crit}} = -8.43 - 2.4\ln(Tu) = 4.3$ [50] based on the wind tunnel turbulence level $Tu = 0.5\%$. Now, because the conformal transformation violates conservation of mass, we apply a correction in the form of $C_{pr,c} = C_{pr} / (q_{\text{rel}} / q_\infty)$ based on equation (4).

The problem is now one of relating the blade nominal angles-of-attack α_n to the corresponding to the azimuthal angles θ. We do this by determining the theoretical angle-of-attack α_0 — using both thin airfoil theory and Xfoil—that produces a zero moment about the strut-blade connection point $(x_c / c = 0.5)$, and we lock this to the experimental azimuthal angle θ_0, which also produces zero moment about the strut-blade connection point. The nominal experimental angle-of-attack/azimuthal-angle relationship is now expressed as:

$$(\alpha_n - \alpha_0) = \tan^{-1}\left(\frac{\sin(\theta+\theta_0)}{\lambda^+ + \cos(\theta+\theta_0)}\right) \approx \frac{(\theta+\theta_0)}{\lambda^+ + 1} + \mathcal{O}(\theta+\theta_0)^3 \qquad (14)$$

where $\lambda^+ = 1.21$ corresponds to $1/(\lambda^+ + 1) = 0.45$, while $\alpha_0 \approx 0°$ and $\theta_0 \approx 26°$.

A side-by-side comparison of static and turbine cases is shown in Figure 14, that shows pressure coefficient data and simulations at corresponding geometric and nominal angles-of-

attack. Immediately evident is the effect of virtual camber, which produces an asymmetric pressure distribution with lower and flatter upper surface pressures on the inner blade surface (also observed in section 4.3). The fact that the turbine blade surface pressure coefficients correspond well to *de facto* physical camber simulations represents the first unambiguous experimental confirmation of high-solidity VAWT blade virtual camber. There are, however, some differences between the data and simulations, for both static and turbine pressure coefficients, that warrant explanation.

For the static case, the suction peaks predicted by Xfoil are somewhat higher than those obtained in the experiments. These differences are possibly due to the experimental setup, which has the blade mounted significantly off-center in the open-jet wind tunnel. This setup, while not ideal, was chosen to minimize, as much as possible, differences between the static and turbine cases. Another source of error may also be related the selection of N_{crit}, which has a strong effect on the leading-edge suction peak, but no attempt was made to vary this parameter. For $\alpha > 10°$, Xfoil simulations show a pressure recovery that is consistent with turbulent trailing-edge separation further upstream than that observed in experiments. An error of this kind is considered to be within the accuracy bounds of Xfoil, owing to the difficulty associated with accurate predictions of turbulent boundary layer separation.

For the turbine case, differences between measurements and simulations are apparent on both the inboard and outboard blade surfaces. Inboard, the simulated leading-edge suction lags the experimental data, and trailing-edge turbulent separation is not correctly predicted. Regarding the latter point, the simulation predicts a separation point that creeps upstream from the trailing-edge with increasing angle-of-attack, while the measurements show a pressure recovery until $\alpha_n > 17.5°$. This is at least partially due to a delay-and-decay effect that is known to occur under dynamic pitching of airfoils that exhibit trailing-edge stall [51,52]. On the outboard surface, the simulations produce a more pronounced stagnation point than the experiments. This may be due to a rotating effect of the blade, which is absent in the simulation, and produces a gentler stagnation region peak in the turbine experiments. Considering the limiting simulation assumptions—namely, steady flow, constant induction factor, conformal transformation, estimation of N_{crit}, and the prediction of turbulent boundary separation, the predictions are more than reasonable.

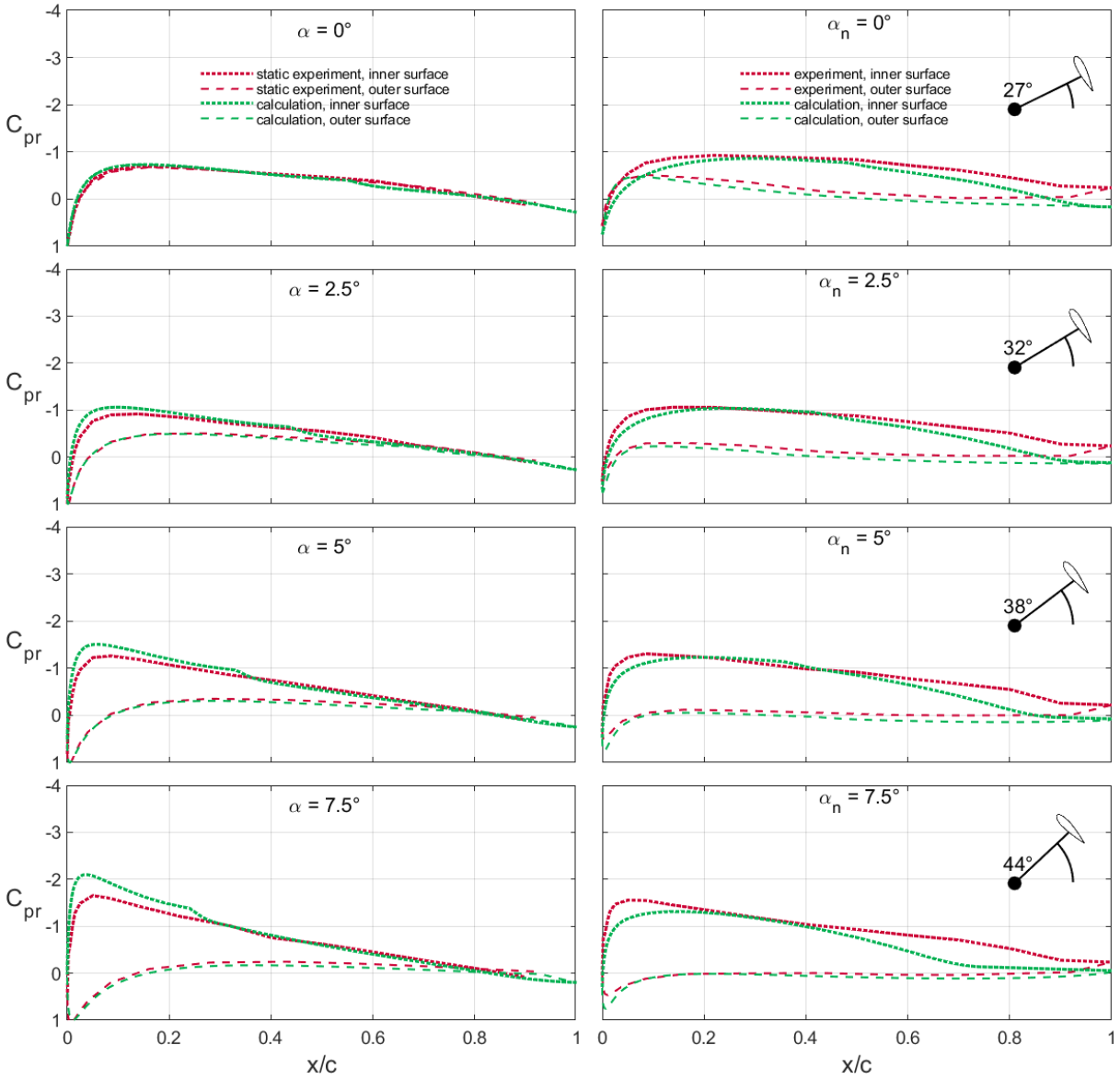

Figure 14. Comparisons of measured pressure coefficients with Xfoil calculations. Left: Static NACA 0021 data and calculations. Right: Turbine data and static NACA 5521 Xfoil-based calculations.

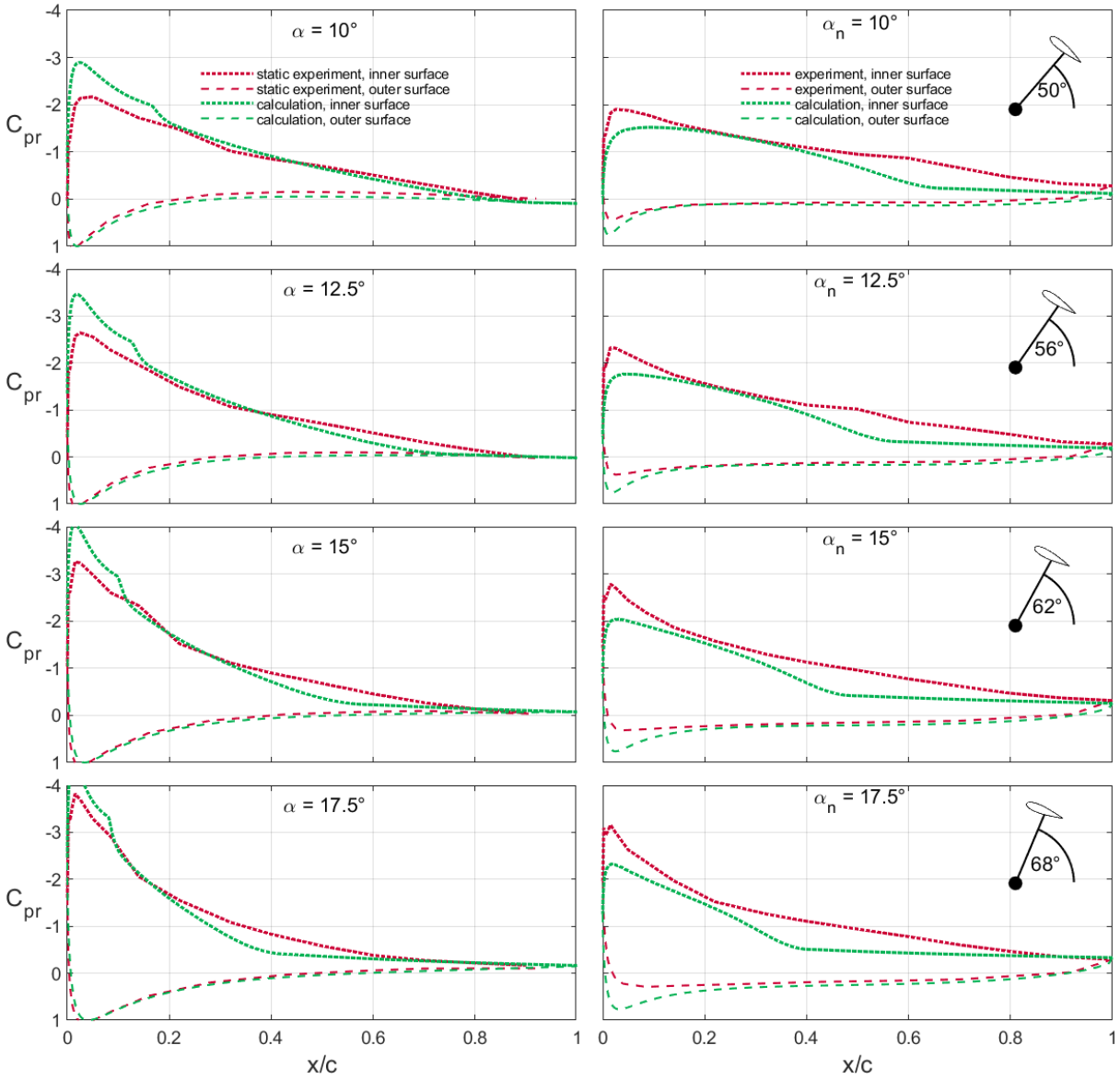

Figure 14. Continued.

Aerodynamic analysis in the downwind quadrants presents a very difficult challenge because: (i) the flow reverses, i.e., from the trailing-edge to the leading-edge in azimuthal segment around $\theta = 180°$; and (ii) it operates either where $W \approx 0$ or in a "dead air" region, i.e., $\bar{U}_i \approx 0$ $(\bar{a} \approx 1)$. The net result is that it is essentially dragged around the azimuth resulting mainly in viscous losses and pitch-down counterclockwise pitching moments.

4.5 Effect of Strut-Blade Connection

Two additional parameters governing turbine performance are the strut-blade connection point x_c / c and the preset angle β. When $\varepsilon << 1$, x_c / c is not a leading parameter, but in our prior

research [18], we observed that a mild peak turbine power peak was attained at $x_c / c \approx 0.5$, which was consistent with the experiments of [53] and the computations of [54]. Moreover, we observed that for $x_c / c = 0.25$—namely, the conventional aerodynamic center in low solidity wind turbines—the turbine barely produced any torque. This was confirmed in the present experiment, where no positive torque could be generated at $U_\infty \le 6$ m/s. There are two reasons for this, and the most important is related to virtual camber. The connection point $x_c / c = 0.25$ produces (i) 5° less virtual camber at the leading-edge, and (ii) large virtual camber, $z'/c(x/c=1) = 8.9\%$, at the trailing-edge (see Figure 15). Hence both leading-edge stall due to smaller "nose droop" and trailing-edge stall due to excessive curvature conspire to decimate the generation of useful torque. The second reason is that the center of pressure moves aft of the connection point, which also acts counter to the turbine rotation. These effects can be offset by introducing a pitch-down (negative) preset angles $\beta < 0$ [18,53] and because these two effects compensate for one another. In the discussion below, we will consider only the effects of connection point.

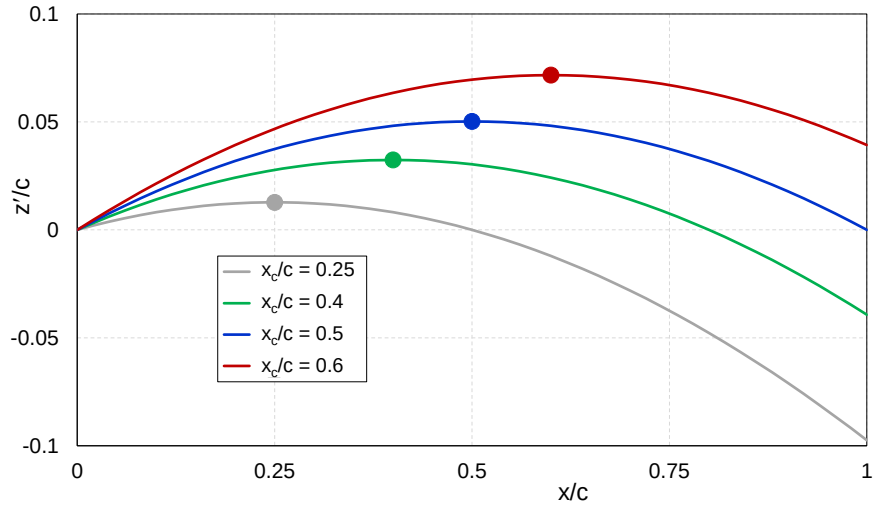

Figure 15. Effect of strut-blade connection points on virtual camber, based on the integration of equation (2) at $\theta = 70°$ for $\varepsilon = 0.75$, $\lambda = 1$, and $\bar{a} = 0.2$.

In the present experiments, comparable total torque was produced at $\lambda = 1$ with connection points at $x_c / c = 0.4$, 0.5 and 0.6, resulting in $C_P = 0.27$, 0.27 and 0.28 respectively. Nevertheless, the mechanisms of torque generation varied significantly, as can be seen in Figure 16. In the first quadrant, the peak torque resulting from blade forces with $x_c / c = 0.4$ is significantly larger than either $x_c / c = 0.5$ and 0.6, which are comparable, but drops

precipitously at $\theta \approx 85°$. Note, however, that the moments developed around the strut connection points increase with increasing x_c / c because the moment-arm increases. The net result is that both $x_c / c = 0.4$ and 0.6 connection points produce higher peak torque than that at $x_c / c = 0.5,$ as can be seen in Figure 17. In the downwind quadrants, the blade forces produce successively higher torque, but the moments produce successively less torque. On balance, the greatest negative downwind torque is produced at $x_c / c = 0.6.$

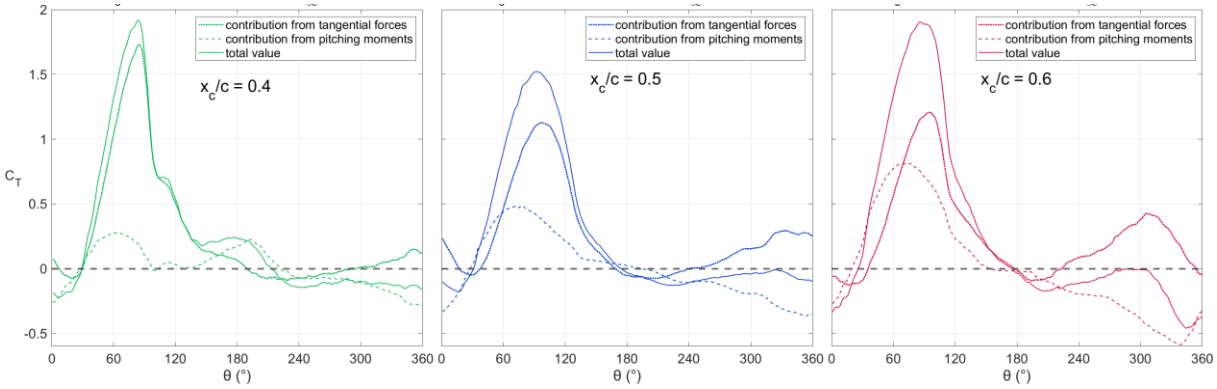

Figure 16. Effect of strut-blade connection point on the development of torque as a function of azimuthal position, for $\lambda = 1.0$, and $U_\infty = 6.1$ m/s.

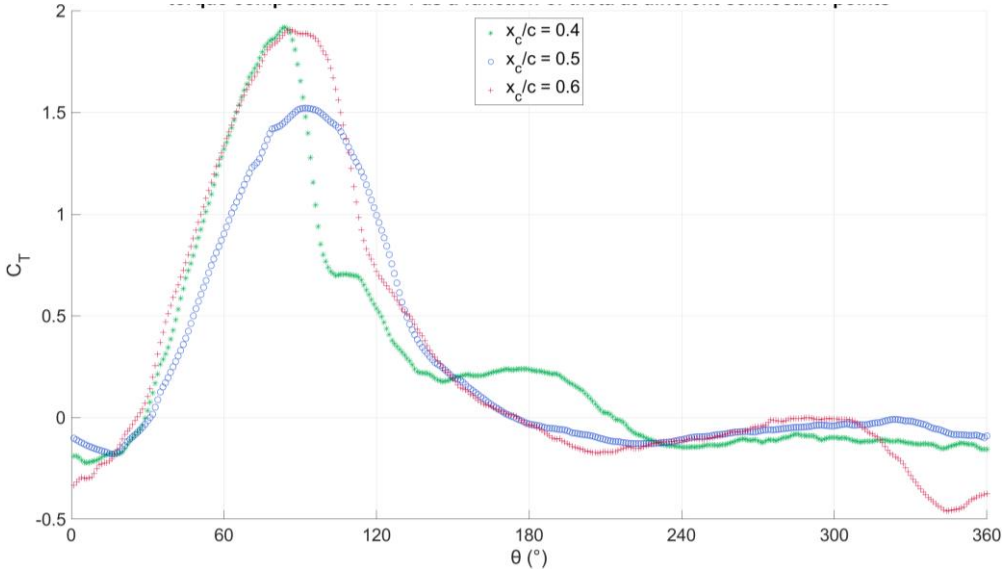

Figure 17. Comparison of total torque developed as a function of azimuthal position, for different strut-blade connection points, extracted from Figure 16.

Surface pressure coefficients at selected angles (Figure 18) illustrate how dynamic stall is affected by the strut-blade connection point. At $\theta = 5°$, the inner surface pressures of $x_c / c = 0.4$ are already lower than those of $x_c / c = 0.5$ and $x_c / c = 0.6$. This disparity increases with increasing azimuthal angle, until the onset of dynamic stall at $\theta \approx 85°$. The primary reason

for this disparity is due to the smaller leading-edge virtual camber with smaller values of x_c / c. At $\theta = 95°$, the aft pressure distribution of $x_c / c = 0.4$ is consistent with an aft vortex, which is the dynamic manifestation of trailing-edge stall [43], and visible up to $\theta = 105°$. Surprisingly, the effect of the strut connection point is not a linear one, because leading-edge stall occurs for $x_c / c = 0.6$ prior to that for $x_c / c = 0.5$, corresponding to approximately 5° in terms of the azimuth. At this stage, the authors do not have a clear explanation for these observations, other than to note that the separation bubble is slightly longer for $x_c / c = 0.6$ and therefore more likely to burst at a lower angle.

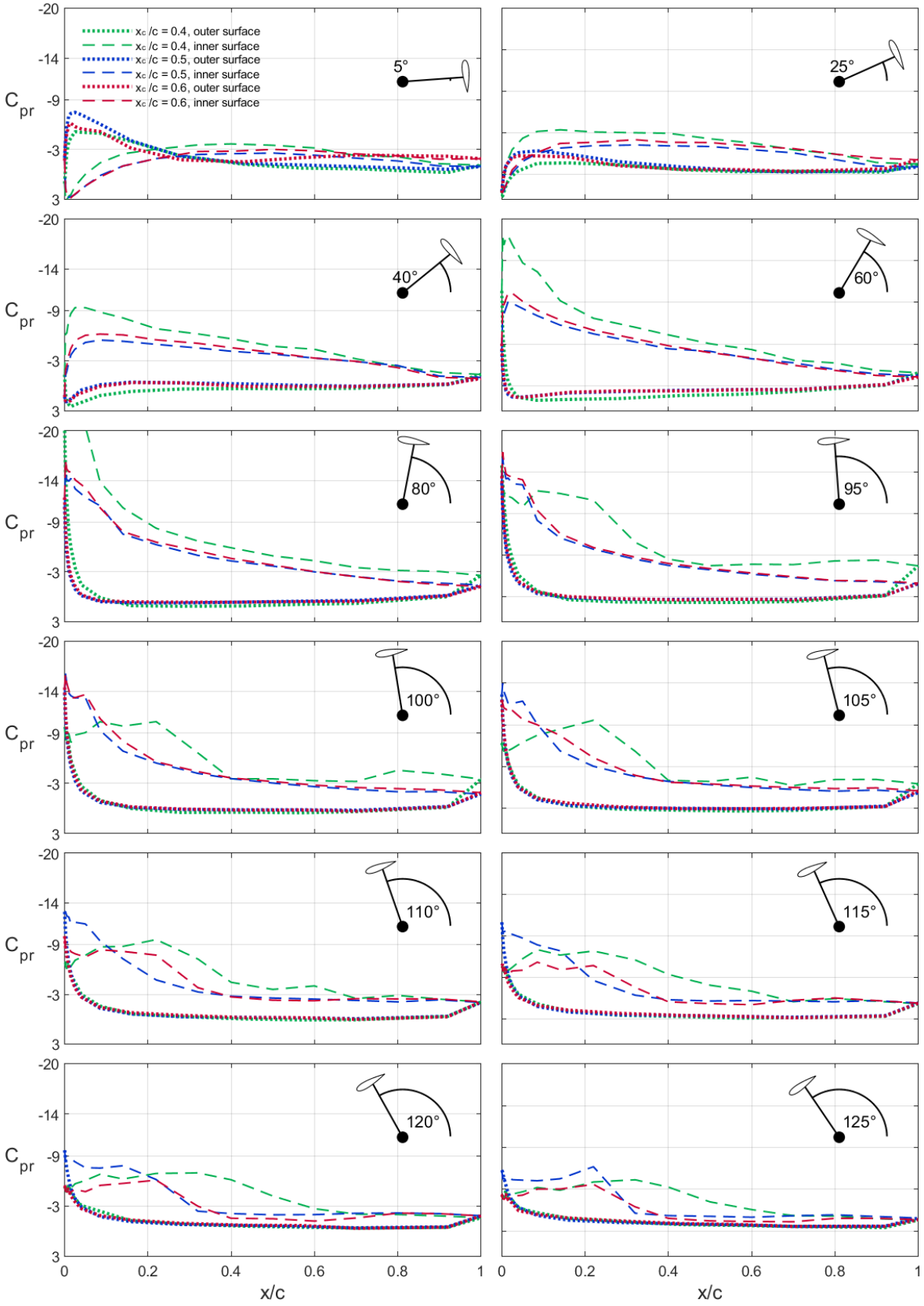

Figure 18. Phase-averaged surface pressure coefficients at peak turbine power for different strut-blade connection points.

4.6 Steady and Unsteady Turbine Loads

Accurate estimates of steady and unsteady loads are important because they directly affect the design of the blades, struts, shaft, and drivetrain. Design optimization, therefore, involves maximizing turbine performance while minimizing the average and unsteady loads. In the discussion below, we compare the $N = 2$ and 3 configurations, as well as the effect of the strut-blade connection point.

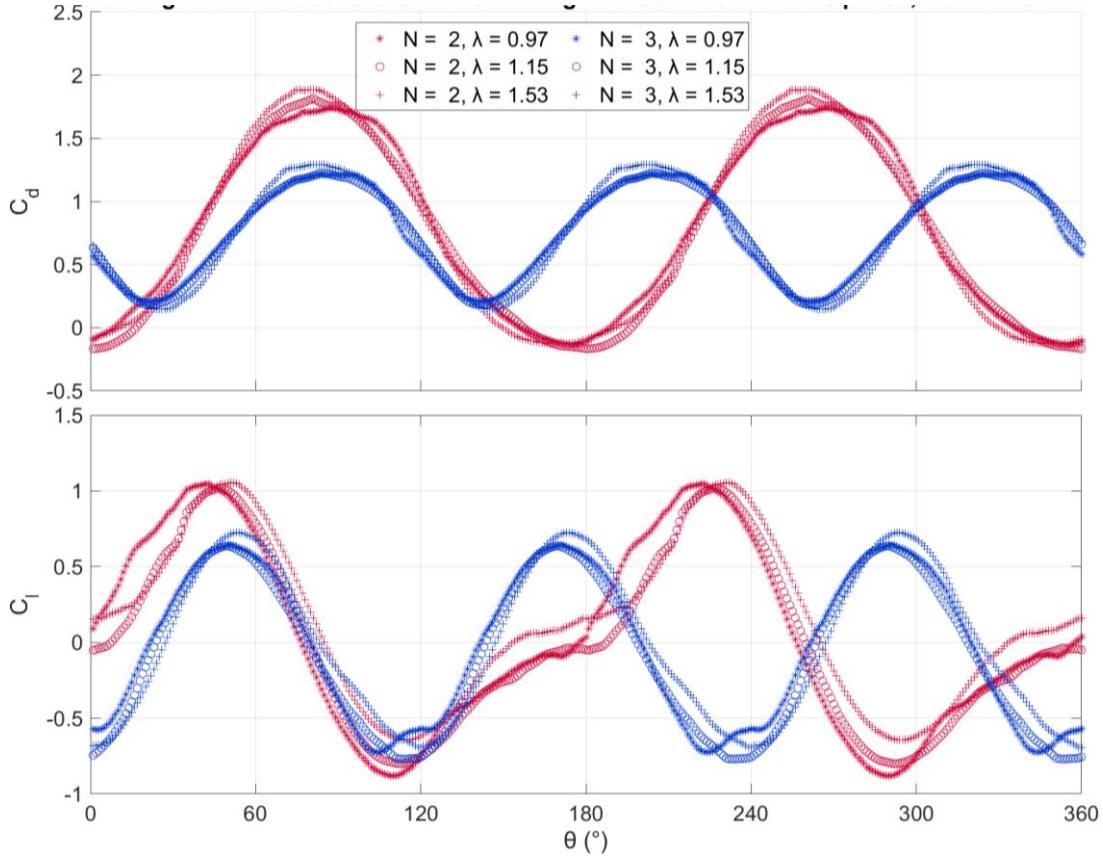

Figure 19. Phase-resolved turbine drag and lateral-force coefficients (upper and lower) for the $N = 2$ and 3 configurations, corresponding to off-design, crossover, and peak power cases, $U_\infty = 6.1$ m/s .

Phase-resolved turbine drag and lateral-force coefficients, $C_d \equiv F_d / q_\infty D$ and $N = 2$, are shown for off-design, crossover, and peak power cases, in Figure 19 (upper and lower plots, respectively). These results are based on summing the contribution of all blades, where the phase-angle represents the position of one (arbitrary) blade. Owing to the fact that these results are based on the blade surface pressure measurements, they do not include drag on the shaft or tip effects. Nevertheless, they clearly illustrate the significant drag coefficient differences between the $N = 2$ and 3 configurations, where the peaks are spaced at 180° and 120°

respectively. The most striking feature is the increase in unsteady drag forces due to decreasing the number of blades. For example, under peak load, the root-mean-square of the unsteady component increases from $C'_d = 0.36$ to 0.69 (i.e., 92%), while the mean values are virtually constant ($C_{\bar{d}} = 0.78$ vs. 0.77). Consideration of a single blade (not shown) shows larger differences in the peak values, but these are offset by thrust components in the downwind quadrants. Lateral force coefficients also show an increase in the unsteady loads, but they are smaller, and the mean values in all cases are small. For example, under peak load, the root-mean-square value increases from $C'_l = 0.48$ to 0.61 (i.e., 27%), while the absolute mean values are both $|C_{\bar{l}}| = 0.04$. It is also evident that the lateral loads are less "sinusoidal" than the drag loads, particularly for the $N = 2$ case. This is because a single blade (not shown) produces two lateral force peaks; a large one at $\theta = 40°$ and a smaller one at $\theta = 180°$.

Table 1. Summary of mean and root-mean-square drag and lateral force coefficients for different strut-blade connection points, $N = 2$, $U_\infty = 6.1$ m/s .

x_c / c	$C_{\bar{d}}$	C'_d	$C_{\bar{l}}$	C'_l
0.4	1.07	0.90	0.26	0.84
0.5	0.79	0.69	0.06	0.61
0.6	1.01	0.75	0.04	0.76

A similar presentation of results illustrating the effect of the strut-blade connection point is shown in Figure 20, for the $N = 2$ configuration (see section 4.5), and the mean and root-mean square values are shown in Table 1. The largest mean and oscillatory drag and lateral-forces are associated with the $x_c / c = 0.4$ case and this is consistent with the large tangential forces developed, which are responsible for the majority of the driving torque (see Figure 16). The large loads were attributed to the smaller leading-edge virtual camber, which precipitated early dynamic stall (see Figure 18). The $x_c / c = 0.6$ unsteady drag forces are larger than the those for $x_c / c = 0.5$ and the reason for this is more subtle. Consideration of a single blade (not shown), shows comparable peak drag coefficients at $\theta \approx 90°$, but the $x_c / c = 0.6$ case produces larger values in the downwind quadrants. Hence the summation for both blades results in larger mean and unsteady values as shown in Table 1. A similar observation is made considering the unsteady lateral force coefficients of a single blade. The $x_c / c = 0.6$ average value is relatively small, however, because a single blade produces a relatively large negative lift force between

$\theta \approx 300°$ and 0°. In light of the fact that similar power coefficients are generated for the the different strut-blade connection points, the connection point $x_c / c = 0.5$ is optimum in terms if mean and unsteady load reduction.

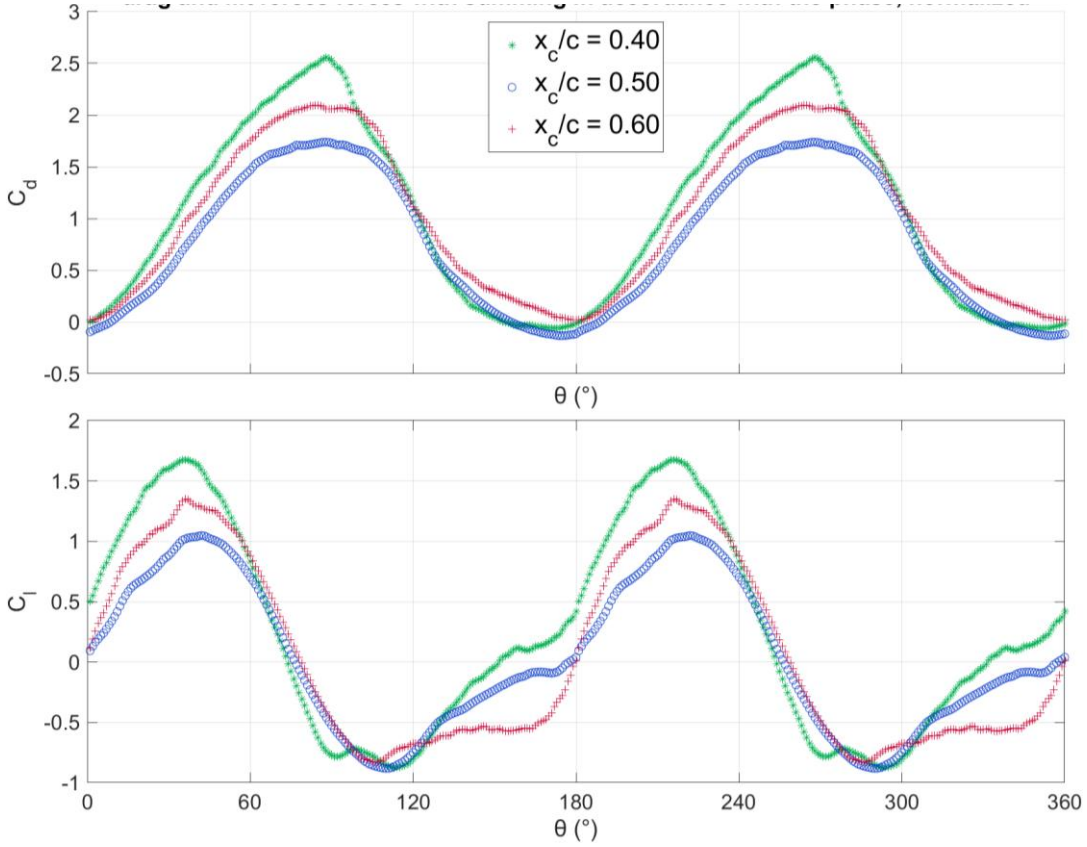

Figure 20. Phase-resolved turbine drag and lateral-force coefficients (upper and lower) for different strut-blade connection points at peak power, $N = 2, U_\infty = 6.1$ m/s .

5 Conclusions

High-solidity VAWT blades have unusual aerodynamics, characterized by dynamic stall and—when the chord-to-radius ratios are large—virtual camber. This experimental research systematically studied the role of both dynamic stall and virtual camber on 2- and 3-bladed turbine models, with NACA 0021 blade profiles, corresponding to chord-to-radius ratios of 0.75 and 0.5, respectively, thereby enforcing constant solidity. Open jet wind tunnel measurements were performed in the wind speed range 4.0 m/s to 8.2 m/s, where phase-resolved blade surface pressures were measured simultaneously with torque, based on dynamometry.

With the strut-blade connection point at 50% of chord, the peak torque and peak power produced by the 2-bladed configuration always exceeded that of the 3-bladed configuration. Consistent with previous investigations by other researchers, virtually all positive torque was developed in the upwind quadrants. Moreover, it was observed that the moment developed around the strut-blade connection point, which is usually neglected, constituted a significant fraction of the total torque developed. In the upwind quadrants, these moments were generally positive, i.e., pitch-up moments, but in the downstream quadrants pitch-down moments produced negative torque. These negative effects can potentially be ameliorated by cyclically cambering the blade.

Three cases were selected for the study of dynamic stall, based on blade surface pressures, namely an off-design case, a crossover case where the performance of both configurations was comparable, and a peak power case. At off-design conditions, no dynamic stall was observed due to a combination of rapid pitch rates and relatively low angles-of-attack associated with the larger blade-wind tip-speed ratios. For the crossover and peak power cases, the two-bladed configuration consistently experienced dynamic stall onset at larger azimuthal angles. This was due to the increased blade pitch rate, which is linearly proportional to the chord-to-radius ratio. For the peak power case, the higher pitchrates associated with the two-bladed configuration led to greater lift forces, which translated to increased turbine performance. The downside of the two-bladed configuration was, as anticipated, unsteady loads on the turbine. At peak power, 92% and 27% greater unsteady drag and lateral force coefficients were recorded for the two-bladed versus the three-bladed configuration.

Virtual camber under peak power was studied by conformally cambering the blade profiles based on the turbine kinematics, performing Xfoil calculations, and then locking the angle-of-attack to the nominal turbine blade angle-of-attack based on zero moment about the

strut-blade connection point. Close correspondence was observed between the calculated cambered blade pressure coefficients and the measured pressure coefficients. These observations were the first unambiguous experimental confirmation of high-solidity VAWT blade virtual camber.

The strut-blade connection point had a profound effect on torque generation. Most surprising, with the connection point at 25% of chord, i.e., the traditional aerodynamic center, the turbine produced almost no useful torque. This was due to a combination of small virtual camber at the leading-edge, large virtual camber at the trailing-edge, and location of the center of pressure aft of the connection point. The cycle-averaged average peak torque values produced by 40%, 50%, and 60% strut-blade connection points were comparable, but the mechanisms were markedly different. For the 40% connection point, greater torque was generated at low azimuthal angles, but dynamic stall occurred prematurely in the first quadrant. For the 60% connection point, the moment about the connection point produced a relatively larger fraction of the total. A strut-blade connection point at 50% was optimum, because it produced the smallest mean an unsteady drag and lateral-force loads.

Acknowledgement

This research was supported by the Israeli Ministry of Energy and Infrastructure, Grant No. 223-17-002.

References

1. Kumar, P.M., Sivalingam, K., Lim, T-C., Ramakrishna, S. and Wei, H., “Review on the Evolution of Darrieus Vertical Axis Wind Turbine: Large Wind Turbines,” Clean Technol., 2019, 1,205-223. https://doi.org/10.3390/cleantechnol1010014
2. Sutherland, H.J., Berg, D.E. and Ashwill. T.D., “A Retrospective of VAWT Technology,” Sandia Report, Jan 2012, https://www.osti.gov/servlets/purl/1035336.
3. Paraschivoiu, I., 2002. Wind turbine design: with emphasis on Darrieus concept. Presses inter Polytechnique.
4. Galinos, C., Larsen, T.J., Madsen, H.A. and Paulsen, U.S., 2016. Vertical axis wind turbine design load cases investigation and comparison with horizontal axis wind turbine. *Energy Procedia*, *94*, pp.319-328.
5. Moore, K.R., Brownstein, I.D. and Ross, H.K., 2024, June. Critical design load case fatigue and ultimate failure simulation for a 10-m H-type vertical-axis wind turbine. In *Journal of Physics: Conference Series* (Vol. 2767, No. 7, p. 072025). IOP Publishing.

6. Mollerstrom, E., Gipe, P., Beurskens, J. and Ottermo, F.," A historical review of vertical axis wind turbines rated 100kW and above," Renewable and Sustainable Energy Reviews, Vol. 105, May 2019, pp 1-13. https://doi.org/10.1016/j.rser.2018.12.022.
7. Paraschivoiu I., "Double-multiple streamtube model for studying vertical-axis wind turbines," AIAA Journal of Propulsion, Vol. 4, No. 4, 1987, pp. 370-377.
8. Tummala, A., Velamati, R.K., Sinha, D.K., Indraja, V. and Krishna, V.H., 2016. A review on small scale wind turbines. Renewable and Sustainable Energy Reviews, 56, pp. 1351-1371.
9. Keisar D, Eilan B, Greenblatt D. "High Pressure Vertical Axis Wind Pump. J Fluids Eng Trans ASME" 2021;143:1–9. https://doi.org/10.1115/1.4049692.
10. Keisar, D., Freger, V. and Greenblatt, D., "Direct wind-powered vertical axis brackish water desalination system," Desalination, Vol. 570, 2024, pp. 117060. https://doi.org/10.1016/j.desal.2023.117060.
11. Ghasemian M, Nejat A. Aero-acoustics prediction of a vertical axis wind turbine using Large Eddy Simulation and acoustic analogy. Energy 2015;88:711–7. https://doi.org/10.1016/j.energy.2015.05.098.
12. Frumkin. R., Pinshow. B. and Kleinhaus. S., "A Review of Bird Migration Over Israel," Journal für Ornithologie, Vol. 136,1995, pp 127-147. https://doi.org/10.1007/BF01651235.
13. Thelander CG, Smallwood KS, Rugge L. "Bird Risk Behaviors and Fatalities at the Altamont Pass Wind Resource Area," Subcontract Rep NREL/SR-500-33829 2003:92 pp. 25-28.
14. Miller MA, Duvvuri S, Brownstein I, Lee M, Dabiri JO, Hultmark M. "Vertical-axis wind turbine experiments at full dynamic similarity". J Fluid Mech 2018;844:707–20. https://doi.org/10.1017/jfm.2018.197.
15. Miller. M.A., Duvvuri. S. and Hultmark, M., "Solidity effects on the performance of vertical-axis wind turbines," Cambridge University Press, 22 September 2021. https://doi.org/10.1017/flo.2021.9.
16. Elkhoury, M., Kiwata, D. and Aoun, E., "Experimental and numerical investigation of a three-dimensional vertical-axis wind turbine with variable-pitch," Journal of Wind Engineering and Industrial Aerodynamics, Vol. 139, Apr 2015, pp. 111-123. http://dx.doi.org/10.1016/j.jweia.2015.01.004.
17. Ma, N., Lei, H., Han, Z., Zhou, D., Bao, Y., Zhang, K., Zhou, L. and Chen, C., "Airfoil optimization to improve power performance of a high-solidity vertical axis wind turbine

at a moderate tip speed ratio," Energy, Vol. 150, 2018, pp. 236-252. https://doi.org/10.1016/j.energy.2018.02.115.

18. Keisar, D., Arava, I. and Greenblatt, D., "Dynamic-Stall-Driven Vertical Axis Wind Turbine: An Experimental Study," Applied Energy, Vol. 365, 2024, 123199. https://doi.org/10.1016/j.apenergy.2024.123199.
19. Jumper EJ, Schreck SJ, Dimmick RL. Lift-curve characteristics for an airfoil pitching at constant rate. J Aircr 1987;24:680–7. https://doi.org/10.2514/3.45507.
20. Strickland JH, Graham GM. "Force coefficients for a NACA-0015 airfoil undergoing constant pitchrate motions". AIAA J 1987;25:622–4. https://doi.org/10.2514/3.9673.
21. Carr LW. Progress in analysis and prediction of dynamic stall. J Aircr 1988;25:6–17. https://doi.org/10.2514/3.45534.
22. Migliore, P. G., Wolfe, W. P., and Fanucci, J. B., "Flow Curvature Effects on Darrieus Turbine Blade Aerodynamics," Journal of Energy, Vol. 4, No. 2, 1980, pp. 49-55. https://doi.org/10.2514/3.62459.
23. Balduzzi, F., Bianchini, A., Maleci, R., Ferrara, G. and Ferrari, L., "Blade design criteria to compensate the flow curvature effects in H-Darrieus wind turbines," Journal of Turbomachinery, Vol. 137, No 1, 2015, p. 011006-1-10. https://doi.org/10.1115/1.4028245.
24. Bianchini, A., Balduzzi, F., Ferrara, G. and Ferrari, L., "Virtual incidence effect on rotating airfoils in Darrieus wind turbines," Energy Conversion and Management, Vol. 111, 2016, pp. 329-338. http://dx.doi.org/10.1016/j.enconman.2015.12.056.
25. Keisar. D., De Troyer. T. and Greenblatt. D., "Concept and operation of a Wind Turbine Driven by Dynamics Stall," AIAA, Vol. 58, June 2020, Number 6. https://doi.org/10.2514/1.J059487.
26. Arava, I., Keisar, D. and Greenblatt, D., 2024. Conformally Decambered Natural Laminar Flow Blades for Vertical-Axis Wind Turbines. AIAA Journal, 62(8), pp.3027-3038.
27. Li, Q.A., Maeda, T., Kamada, Y., Murata, J., Shimizu, K., Ogasawara, T., Nakai, A. and Kasuya, T., 2016. Effect of solidity on aerodynamic forces around straight-bladed vertical axis wind turbine by wind tunnel experiments (depending on number of blades). Renewable Energy, 96, pp. 928-939 .https://doi.org/.1037//0033-2909.I26.1.78.
28. Dumitrescu, H. and Cardos, V., 1998. Wind turbine aerodynamic performance by lifting line method. International Journal of Rotating Machinery, 4(3), pp.141-149.
29. Bianchini, A., Marten, D., Tonini, A., Balduzzi, F., Nayeri, C.N., Ferrara, G. and Paschereit, C.O., 2018. Implementation of the "virtual camber" transformation into the

open source software QBlade: validation and assessment. *Energy Procedia*, *148*, pp.210-217.

30. Müller-Vahl HF, Strangfeld C, Nayeri CN, Paschereit CO, Greenblatt D. "Control of thick airfoil, deep dynamic stall using steady blowing". AIAA J 2015;53:277–95. https://doi.org/10.2514/1.J053090.
31. Buchner A-J, Soria J, Honnery D, Smits AJ. "Dynamic stall in vertical axis wind turbines: scaling and topological considerations". J Fluid Mech 2018;841:746–66. https://doi.org/10.1017/jfm.2018.112.
32. Le Fouest, S. and Mulleners, K., "The dynamic stall dilemma for vertical-axis wind turbines," Renewable Energy, Vol. 198, 2022, pp. 505-520. https://doi.org/10.1016/j.renene.2022.07.071.
33. Rezaeiha A, Montazeri H, Blocken B. Towards optimal aerodynamic design of vertical axis wind turbines: Impact of solidity and number of blades. Energy 2018;165:1129–48. https://doi.org/10.1016/j.energy.2018.09.192.
34. Guo, Y., Li, X., Sun, L., Gao, Y., Gao, Z. and Chen, L., "Aerodynamic analysis of a step adjustment method for blade pitch of a VAWT," Journal of Wind Engineering and Industrial Aerodynamics, Vol. 188, 2019, pp. 90-101. https://doi.org/10.1016/j.jweia.2019.02.023.
35. Zanforlin S, Deluca S. Effects of the Reynolds number and the tip losses on the optimal aspect ratio of straight-bladed Vertical Axis Wind Turbines. Energy 2018;148:179–95. https://doi.org/10.1016/j.energy.2018.01.132.
36. Brusca S, Lanzafame R, Messina M. "Design of a vertical-axis wind turbine: how the aspect ratio affects the turbine's performance". Int J Energy Environ Eng 2014;5:333–40. https://doi.org/10.1007/s40095-014-0129-x.
37. Carmichael, B.H., "Low Reynolds number airfoil survey," Volume 1, NASA-CR-165803-VOL-1, 1981. https://ntrs.nasa.gov/citations/19820006186.
38. Lissaman, P.B.S., 1983. Low-Reynolds-number airfoils. Annual review of fluid mechanics, 15(1), pp.223-239.
39. Rathore, M.K., Agrawal, M. and Baredar, P., 2021. Pitch control mechanism in various type of vertical axis wind turbines: a review. Journal of Vibration Engineering & Technologies, 9(8), pp.2133-2149.
40. Aubrun, S., Leroy, A. and Devinant, P., 2017. A review of wind turbine-oriented active flow control strategies. Experiments in Fluids, 58(10), p.134.

41. Lachenal, X., Daynes, S. and Weaver, P.M., 2013. Review of morphing concepts and materials for wind turbine blade applications. Wind energy, 16(2), pp.283-307.
42. Baghdadi, M., Elkoush, S., Akle, B. and Elkhoury, M., "Dynamic shape optimization of a vertical-axis wind turbine via blade morphing technique," Renewable Energy, Vol. 154, 2020, pp. 239-251. https://doi.org/10.1016/j.renene.2020.03.015.
43. Müller-Vahl, H., Strangfeld, C., Nayeri, C.N., Paschereit, C.O. and Greenblatt, D., "Thick airfoil dynamic stall," in "Wind Energy – Impact of Turbulence," Eds. M. Hölling, J. Peinke and S. Ivanell, Springer, pp. 35-40, 2013. https://doi.org/10.1007/978-3-642-54696-9_6.
44. Zhu, H., Hao, W., Li, C., Ding, Q. and Wu, B., "A critical study on passive flow control techniques for straight-bladed vertical axis wind turbine," Energy, Vol. 165, Part A, 2018, pp. 12-25. https://doi.org/10.1016/j.energy.2018.09.072.
45. Syawitri, T.P., Yao, Y., Yao, J. and Chandra, B., "A review on the use of passive flow control devices as performance enhancement of lift‐type vertical axis wind turbines," Wiley Interdisciplinary Reviews: Energy and Environment, Vol 11, No. 4, 2022, p.e435. https://doi.org/10.1002/wene.435.
46. Rezaeiha, A., Montazeri, H. and Blocken, B., "Active flow control for power enhancement of vertical axis wind turbines: Leading-edge slot suction," Energy, Vol. 189, 2019, p. 116131. https://doi.org/10.1016/j.energy.2019.116131.
47. Greenblatt, D., Schulman, M. and Ben-Harav, A., 2012. Vertical axis wind turbine performance enhancement using plasma actuators. Renewable Energy, 37(1), pp.345-354.
48. Ben-Harav, A. and Greenblatt, D., 2016. Plasma-based feed-forward dynamic stall control on a vertical axis wind turbine. Wind Energy, 19(1), pp.3-16.
49. Drela, M. 1989 XFOIL: An analysis and design system for low Reynolds number airfoils. In Low Reynolds Number Aerodynamics, pp. 1–12. Springer.
50. Van Ingen, J., 2008, June. The eN method for transition prediction. Historical review of work at TU Delft. In *38th Fluid Dynamics Conference and Exhibit* (p. 3830).
51. Goman, M. and Khrabrov, A., "State-space representation of aerodynamic characteristics of an aircraft at high angles-of-attack," Journal of Aircraft, Vol. 31, No. 5, 1994, pp. 1109-1115. https://doi.org/10.2514/3.46618.
52. Williams, D.R., Reißner, F., Greenblatt, D., Müller-Vahl, H. and Strangfeld, C., 2017. Modeling lift hysteresis on pitching airfoils with a modified Goman–Khrabrov model. AIAA Journal, 55(2), pp. 403-409.

53. Fiedler AJ, Tullis S. “Blade offset and pitch effects on a high solidity vertical axis wind turbine”. Wind Eng 2009;33:237–46. https://doi.org/10.1260/030952409789140955.
54. Bianchini, A., Balduzzi, F., Ferrara, G. and Ferrari, L., 2016, June. Influence of the blade-spoke connection point on the aerodynamic performance of Darrieus wind turbines. In Turbo Expo: Power for Land, Sea, and Air (Vol. 49873, p. V009T46A012). American Society of Mechanical Engineers.